# Effects of postglacial seawater intrusion on sediment geochemical characteristics in the Romanian sector of the Black Sea

**Livio Ruffine[*1], Christian Deusner[*2], Matthias Haeckel[2], Elke Kossel[2], Samuel Toucanne[1], Sandrine Chéron[1], Audrey Boissier[1], Mark Schmidt[2], Jean-Pierre Donval[1], Florian Scholz[2], Vivien Guyader[1], Stéphan Ker[1] and Vincent Riboulot[1]**

[*] These two authors contributed equally to this work
[1] IFREMER, Département Ressources physiques et Ecosystèmes de fond de Mer (REM), Unité des Géosciences Marines, 29280 Plouzané, France
[2] GEOMAR Helmholtz Centre for Ocean Research Kiel, Wischhofstr. 1-3, D-24148 Kiel, Germany

Corresponding author: Email: livio.ruffine@ifremer.fr

Tél : + 33 2 98 22 48 88

## Abstract

Pore water and sediment geochemistry in the western Black Sea were investigated on long *Calypso* piston core samples. Using this type of coring device facilitates the recovery of the thick sediment record necessary to analyze transport-reaction processes in response to the postglacial sea-level rise and intrusion of Mediterranean salt water 9 ka ago, and thus, to better characterize key biogeochemical processes and process changes in response to the shift from lacustrine to marine bottom water composition. Complementary data indicate that organic matter degradation occurs in the upper 15 m of the sediment column. However, sulfate reduction coupled with Anaerobic Methane Oxidation (AOM) is the dominant electron-accepting process and characterized by a shallow Sulfate Methane Transition Zone (SMTZ). Net silica dissolution, total alkalinity (TA) maxima and carbonate peaks are found at shallow depths. Pore water profiles clearly show the uptake of $K^+$, $Mg^{2+}$ and $Na^+$ by, and release of $Ca^{2+}$ and $Sr^{2+}$ from the heterogeneous lacustrine sediments, which is likely controlled by chemical reactions of silicate minerals and changes in clay mineral composition. Iron ($Fe^{2+}$) and manganese ($Mn^{2+}$) maxima largely coincide with $Ca^{2+}$ peaks and suggest a close link between $Fe^{2+}$, $Mn^{2+}$ and $Ca^{2+}$ release. We hypothesize that the $Fe^{2+}$ maxima below the SMTZ result from deep $Fe^{3+}$ reduction linked to organic matter degradation, either driven by DOC escaping from the shallow sulfate reduction zone or slow degradation of recalcitrant POC. The chemical analysis of dissolved and solid iron species indicates that iron is essentially associated with clay minerals, which suggests that microbial iron reduction is influenced by clay mineral composition and bioavailability of clay mineral-bound Fe(III). Overall, our study suggests that

postglacial seawater intrusion plays a major role in shaping redox zonation and geochemical profiles in the lacustrine sediments of the Late Quaternary.

*Keywords:*
Black sea, clay minerals, Danube delta, gas seeps, iron reduction, methane oxidation, sulfate reduction,

## Introduction

The Black Sea has been investigated for decades, primarily because it is the largest anoxic basin on Earth and it represents a large hydrocarbon-producing province (Kosarev, 2007; Robinson et al., 1996; Robinson, 1997). Previous investigations were diverse and integrated physical oceanography, petroleum geology, tectonics, paleoceanography, hydrology, and marine biology and ecosystem studies to reconstruct the history of the basin, capture its current dynamics and preserve its environmental quality and biodiversity. The Black Sea is connected to the Atlantic Ocean through the Marmara and the Mediterranean seas, and is characterized by two water masses: a salty water mass at the bottom supplied from the ocean, and a fresh water mass at the surface delivered by the rivers. The Black Sea hosts a large number of vigorous methane-rich seeps from the continental shelf to the deepest part of its basins that release gas high into the water column (Hillman et al., 2018a; Kessler et al., 2006a; Kessler et al., 2006b; Naudts et al., 2006; Roemer et al., 2012; Schmale et al., 2010a; Schmale et al., 2005; Schmale et al., 2011; Schmale et al., 2010b). These seeps play a pivotal role in the Black Sea methane cycling (Pape et al., 2008; Reeburgh et al., 1991; Schmale et al., 2010a) and are the major methane source responsible for the high concentrations measured in the water column (Greinert et al., 2006; Greinert et al., 2010; Reeburgh, 2007). However, a significant amount of methane generated in the sediment does not reach the water column (Wallmann et al., 2006) as it is partly stored as gas hydrates (Blinova et al., 2003; Bohrmann et al., 2003; Heeschen et al., 2011; Ker et al., 2019; Popescu et al., 2007; Zander et al., 2017) or oxidized within the anoxic sediment (Holmkvist et al., 2011; Jorgensen et al., 2004; Jorgensen et al., 2001; Meister et al., 2013; Niewohner et al., 1998; Reeburgh et al., 1991; Regnier et al., 2011; Reitz et al., 2011; Wallmann et al., 2006; Zander et al., 2020).

The chemical composition of pore water in the anoxic Black Sea surface sediments is significantly affected by the onset of the intrusion of seawater into the basin approximately 9 ka BP (Soulet et al., 2011b), giving rise to transient-state diffusion profiles and non-equilibrium

chemical conditions. Thus, the natural setting is ideal to provide mechanistic insight and characterize dynamics of important diagenetic processes related to mineral dissolution, alteration or secondary mineral formation. Previous geochemical studies have shown that the sedimentary column of the Black Sea is highly reactive and particulate organic carbon (POC) degradation largely occurs in the upper part of the sediment (Egger et al., 2016; Henkel et al., 2012; Schouten et al., 2001). Methanogenesis, organoclastic sulfate reduction (SR) and anaerobic oxidation of methane (AOM) represent key reactions central to the Black Sea carbon cycling amongst the broad range of redox reactions that commonly lead to the vertical zonation of the sediment. Microbial iron and manganese reduction below the Sulfate Methane Transition Zone (SMTZ) contribute to organic matter degradation, and it is a topic of ongoing discussion if the reactions are driven by methane oxidation or the turnover of other organic or inorganic substrates (Egger et al., 2016). Previous studies have demonstrated the strong link between carbon, sulfur, iron and phosphate cycling and also suggest a strong coupling between methane turnover and silicate weathering (Aloisi et al., 2004a; Aloisi et al., 2004b; Egger et al., 2017; Egger et al., 2016; Henkel et al., 2012; Reitz et al., 2011; Wallmann et al., 2006). All of the aforementioned microbially influenced geochemical processes can significantly alter the chemistry of pore waters and sediment mineral composition.

Northern hemisphere climate variations during the last glacial and the Holocene strongly influenced the size of continental ice sheets and glaciers, and the global sea level. This affected the water level of the Black Sea/Lake as well as the sources and intensity of riverine input, resulting in varying accumulation of terrigeneous sediments from different sources and with different rates (Huvaj and Huff, 2016; Özsoy and Ünlüata, 1997; Piper and Calvert, 2011; Stoffers and Muller, 1972; Wegwerth et al., 2016). In addition to input dynamics, local lithostratigraphy is influenced by internal dynamics resulting from sediment mobilization and re-deposition, slumping and slope failure events and the complicated functioning of the Danube deep sea fan (Constantinescu et al., 2015; Hillman et al., 2018b; Popescu et al., 2004; Xu et al., 2018), which connects the upper shelf with the deep basin. Historically, three sedimentary units were identified describing the general stratigraphy of Late Pleistocene and Holocene sediments in the Black Sea (e.g., Degens and Ross, 1972): a microlaminated coccolith ooze (Unit I, since ca. 2.76 ka BP; Lamy et al., 2006); an organic matter rich sapropel (Unit II, since ca. 8.5 ka BP; Soulet et al., 2011); and (Unit III) a banded lacustrine lutite. Recent efforts provided more detailed lithological and chronostratigraphical information from different parts of the Black Sea (e.g. Lamy et al., 2006; Kwiecien et al., 2008; Soulet et al., 2011; Nowaczyk et al., 2012; Soulet et al., 2018), still highlighting the complexity of building age model frameworks due to

problems of constraining reservoir ages and sediment input on local and regional scales (Kwiecien et al., 2008; Soulet et al., 2011). The Danube River is considered to be the major source of sediment to the north-western margin of the Black Sea (Lericolais et al., 2013), especially during the ca. 32-17 ka period (Martinez-Lamas et al., 2020). Over this period, the river was characterized by high flood activity supplying huge amounts of sediment to the margin and the deep basin. Martinez-Lamas et al. (2020) demonstrated that the major sources of sediment have changed over that period, primarily because of the dynamics of the Alpine Ice sheets (AIS), but also that of the Fennoscandian Ice Sheet (FIS)(Soulet et al., 2013). Changes in the chemical composition and mineralogy of the deposited sediment are controlled by the relative inputs from the Danube tributaries connected to three main zones of the drainage basin (Martinez-Lamas et al., 2020). Thus, unlike the North-Eastern Alps, the Carpathians and the Dinarides are characterized by an abundance of kaolinite, and a low dolomite content. The Alpine glaciers provide illite-rich sediment, with a significant amount of smectite, chlorite, and dolomite; the two latter being mainly supplied from the inner Alpine.

In 2015, a study in the Romanian sector of the Black Sea has been undertaken on board the R/V Pourquoi pas? to map the distribution of fluid seeps and gas hydrates in the area, and to identify relationships between fluid migration and sediment destabilization, which could be observed from features apparently related to slumping and slope failure (Ballas et al., 2018; Riboulot et al., 2017; Riboulot et al., 2018). Special attention was also given to the understanding of the dynamics of the gas hydrate deposits (Ker et al., 2019), and the occurrence of multiple BSRs (Zander et al., 2017). The area was previously investigated, mainly to reconstruct its past climate and the functioning of the Danube delta (Constantinescu et al., 2015; Major et al., 2006; Popescu et al., 2006; Soulet et al., 2010). However, unlike other sectors of the Black Sea (Aloisi et al., 2004a; Aloisi et al., 2004b; Reitz et al., 2011; Wallmann et al., 2006), there are only few studies in this dynamic area (e.g. Jorgensen et al. 2001, Knab et al. 2009, Egger et al. 2016) aimed to document geochemical processes in response to seawater intrusion and gas seepage. Hence, the purpose of this study is to contribute towards filling this gap by integrating geochemical analyses of pore water and sediment samples to decipher the coupling of element cycling in the upper tens of meters of the sedimentary column.

## Description of the study area

Our study area is located in the Romanian water sector (Fig. 1) at the eastern part of the main Danube canyon, where several other canyons have developed. In this area, evidence for

sediment instability and mass movement was found during cruise MSM-34 in 2013 (Bialas et al., 2014; Haeckel et al., 2015) and GHASS cruise in 2015 (doi: 10.17600/15000500). Acoustic surveys of the water column on both cruises showed that this area is characterized by a large number of widespread gas expulsion sites at the seafloor, bubbling up to several tens to hundreds of meters into the water column (Riboulot et al., 2017). Sites of intense gas seepage indicate strong upward methane migration and discharge in and from the anoxic Black Sea sediments. Accordingly, they have served for guiding coring operation during the GHASS cruise. The cores were collected from water depths between 240 m and 822 m. Core GAS-CS01 was collected at the shelf edge, and GAS-CS07, 08 and 14 along a crest, and the remaining ones on landslide scars or small seafloor depressions. Riboulot et al. (2018) have shown that the pattern of the seep distribution is related to the gas hydrate stability zone (GHSZ). Indeed the gas flares are primarily located on the shelf and at the upper border of the GHSZ. Within the GHSZ seeps are positioned only at the rim of landslide scars, and at specific location where faults reach the seafloor (Ker et al., 2019).

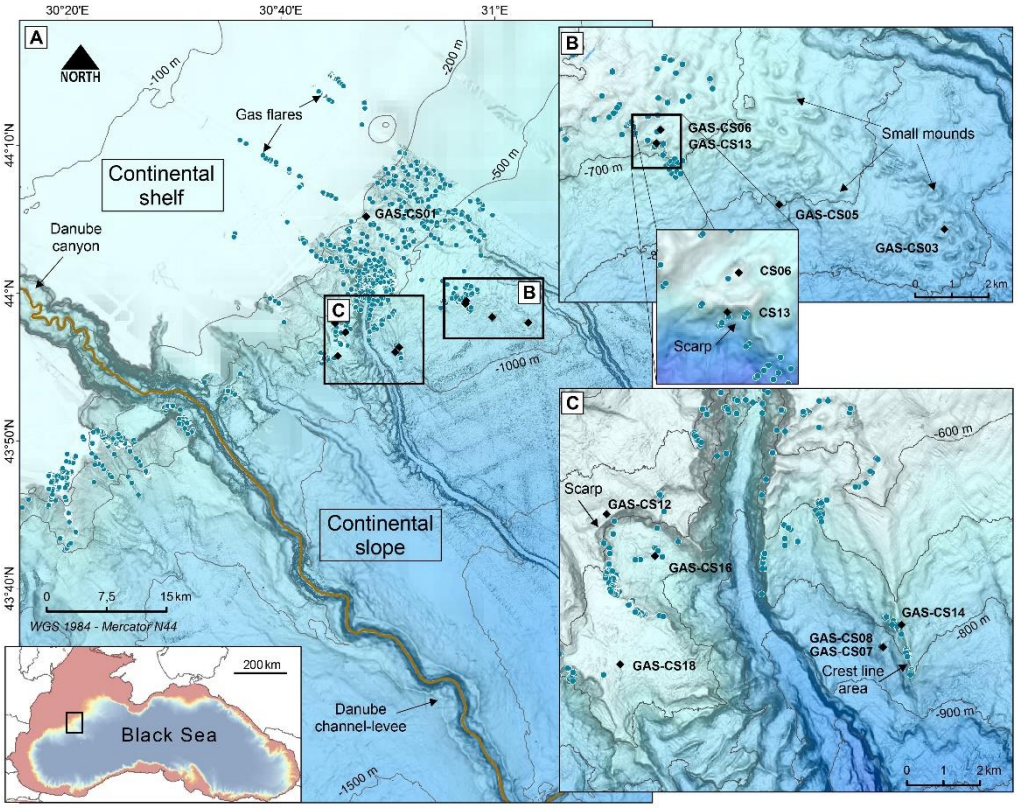


Fig. 1: A) Bathymetric map of the Romanian sector of the Black Sea showing the Danube canyon and the location of all cores recovered on the continental slope. The blue dots highlight the acoustic gas flares identified in the water column during the GHASS cruise (Riboulot et al., 2017). B and C) Detailed views of the study area with location of the cores. Core positioning was guided by the presence of gas flares, or other indications or topographical features attributable to potential presence of shallow gas hydrates.

## Sampling and analyses

*Coring and sampling*

During the GHASS cruise, the coring locations together with Penfeld measurements were selected from previous acoustic and seismic surveys. A Calypso piston-corer was deployed to collect long sediment cores with a length of up to ~35m. A total of 11 cores were collected (Table 1) for geochemical, geophysical and geotechnical analysis. Once retrieved, the Calypso cores were cut into 1m long round sections and transferred to the shipboard laboratory for pore water sampling and processing at sea bottom temperature. The sediment cores were sampled for pore water analyses immediately after the recovery.

Table 1: List of cores recovered and sampled for pore water analyses

| Core name | Coordinates | Length/ cm | Water depth/ m |
|---|---|---|---|
| **GAS-CS01** | N44°05.188'; E30° 47.961' | 3337 | **240** |
| **GAS-CS03** | N43°58.030'; E31° 03.107' | 2246 | **842** |
| **GAS-CS05** | N43°58.3944'; E30° 59.7349' | 1179 | **794** |
| **GAS-CS06** | N43°59.4985'; E30°57.3139' | 1970 | **650** |
| **GAS-CS07** | N43°56.048'; E30°50.6635' | 1234 | **822** |
| **GAS-CS08** | N43°56.048'; E30°50.6635' | 2080 | **821** |
| **GAS-CS12** | N43°57.994'; E30°45.020' | 2464 | **547** |
| **GAS-CS13** | N43°59.298'; E30°57.234' | 1381 | **660** |
| **GAS-CS14** | N43°56.361'; E30°51.044' | 542 | **738** |
| **GAS-CS16** | N43°55.450'; E30°45.427' | 2564 | **685** |
| **GAS-CS18** | N43°55.777'; E30°45.301' | 2740 | **638** |

Pore water was sampled using two different methods. Rhizon samplers were used as long as the sediment was soft enough to insert the plastic tip of the sampler. A Rhizon sampler (Rhizosphere Research Products, Netherlands) is a narrow elongated cylindrical filter (0.2 µm pore size; 5 cm long; 130 µL volume) with a stiff plastic core (Seeberg-Elverfeldt et al., 2005). Prior to use, the samplers were conditioned in distilled water ("MilliQ") for several hours. Rhizon samplers are used to draw fluid from the sediment under vacuum, which is applied by attaching the samplers to 10 mL or 20 mL all-plastic syringes. The sampling took less than 12 hours. In addition to using Rhizon samplers, pore water was extracted using a pore water squeezer with $N_2$ gas of up to 5 bar as pressurizing agent and filtering the pore water through

0.2 µm Nuclepore cellulose acetate filters. The use of a second pore-water sampling method was necessary to recover sufficient water volumes for all analyses. Sediment samples for pore water pressing and sediment analysis were taken directly after recovery of the core from round sections or opened core halves. A 4-cm thick slice of sediment was removed from the working half at either the top or the bottom of the core section. Subsamples of the wet sediment were taken for measurement of sediment porosity, as well as for chemical and mineralogical analyses.

*Geochemical analysis*

Aliquots of the extracted pore water were sub-sampled for various onboard and shore-based analyses. Analyses for the nutrients $NH_4^+$, $PO_4^{3-}$, $SiO_4^{4-}$ as well as $H_2S$ were completed onboard using a Hitachi UV/VIS spectrophotometer. The respective chemical analyses followed standard procedures (Grasshoff et al., 1999), i.e. $NH_4^+$ was measured as indophenol blue, $PO_4^{3-}$ and $SiO_4^{4-}$ as molybdenum blue, and $H_2S$ as methylene blue. Total alkalinity (TA) was determined by titration with 0.02 N HCl using a mixture of methyl red and methylene blue as indicator. IAPSO seawater standard was used for calibration. $Cl^-$, $Br^-$ and $SO_4^{2-}$ concentrations were determined by ion chromatography (METROHM 761 Compact). Cations were analyzed using ICP-OES (VARIAN 720-ES). Subsamples for ICP-OES analysis were acidified with 20 µl of conc. suprapure $HNO_3$ per 2 ml of porewater sample (i.e., pH < 1). All samples for shore-based analyses were stored refrigerated. Further analytical details, including analytical accuracies, precisions and detection limits, can be found in a previous study (Haffert et al., 2013).

Dissolved methane concentration was determined from a poisoned aliquot of wet sediment (10 µL of $NaN_3$) by head-space coupled gas chromatography (Agilent GC-7890A coupled with a sampler HP7694). Stable carbon isotopic ratio of methane ($\delta^{13}C/^{12}C$) was measured by using a continuous flow isotope ratio mass spectrometer (Thermo MAT253). Prior to oxidation of methane in a 1150 °C furnace, methane was separated from other gases in a coupled Thermo Trace GC (carrier gas: He; packed column: ShinCarbon, 1.5 m). Stable isotope ratios are reported in the δ-notation with respect to Vienna Pee Dee Belemnite (VPDB). Analytical precision of the reported isotopic composition is ± 0.3 ‰.

Wet sediment was collected for shore-based porosity, carbonate and element CNS analyses. Analyses were carried out using a EURO Element Analyzer (C/N/S configuration), prior and after removal of inorganic carbon with 1 M HCl. The analytical data are presented in

percent of the total weight of dried sediment with an accuracy of 3%. Bulk chemical composition analysis of the sediment was carried out with a wavelength dispersive X-ray fluorescence spectrometer S8-Tiger from BRUKER. Mineral composition analysis of sediment samples was performed by X-ray diffractometry (XRD) using a D8 Advance model from BRUKER. Qualitative analysis of the diffraction pattern was carried out with the EVA software (BRUKER) for phase identification of unknown samples, while quantitative analyses were performed according to the Rietveld refinement method with the program TOPAS (BRUKER). Specific analyses were done to determine the clay mineral content according to a validated method commonly used for clay analysis (Holtzappel, 1985). The clay content was calculated by applying specific coefficients for the identified clays minerals (Underwood and Pickering, 1996). The results are given with an uncertainty of 10%. X-ray absorption near edge structure spectroscopy (XANES) (Calvin, 2013) was performed to investigate the mineralogy and the oxidation state of the mineral-bound iron. XANES spectra were recorded at beamline P64 of the synchrotron radiation source PETRA (Caliebe et al., 2019), which is operated by the Helmholtz research centre DESY in Hamburg, Germany. For the determination of the mineralogy, a set of reference spectra of iron-containing silicates (augite, biotite, montmorillonite, nontronite and olivine), oxides (ferrihydrite, goethite and hematite) and an iron sulfide (pyrite) were measured. The software package Athena (Ravel and Newville, 2005) was then used for linear fitting of the reference spectra to the XANES spectra of sediments from core GAS-CS01 (Scholz et al., 2016). The mean oxidation state of the sediments (fraction of ferric Fe, Fe(III)/$\sum$(Fe)) was obtained from the centroid position of the pre-edge structure (Scholz et al., 2016; Wilke et al., 2001).

# Results

*Geochemical composition of pore water*

Pore water profiles of dissolved elements ($Cl^-$, $SO_4^{2-}$, $Ca^{2+}$, $Mg^{2+}$, $Na^+$, $K^+$, $Ba^{2+}$, $Sr^{2+}$, $NH_4^+$, $Br^-$, $PO_4^{3-}$, $SiO_4^{4-}$, $HS^-$, $Fe^{2+}$ and $Mn^{2+}$) and total alkalinity (TA) are presented in Fig.2. Chemical and isotope data of methane ($CH_4$) are shown in Fig.3, and sediment geochemical composition and mineralogy in Fig.4 and 5. Overall, pore water geochemical profiles show similar trends, and there is no significant effect of water depth or sample location on pore water profiles in Calypso cores retrieved on the slope, both close to and far from the shelf, for $Cl^-$, $SO_4^{2-}$, $Ca^{2+}$, $Mg^{2+}$, $Na^+$, $K^+$, $Ba^{2+}$, $Sr^{2+}$. However, pore water profiles from cores GAS-CS13 and GAS-CS14 appear as shifted and show significantly lower concentrations of dissolved

elements compared to the other cores. The concentrations of $Cl^-$, $Mg^{2+}$, $Na^+$, $K^+$, TA and $Br^-$ decrease non-linearly with depth, resulting in profiles with a concave-down curvature, whereas concentrations of $Ca^{2+}$, $Ba^{2+}$, $NH_4^+$, and $Sr^{2+}$ increase to a clear and pronounced maximum followed by a decrease with increasing depth. Among major cations $K^+$, $Mg^{2+}$ and $Na^+$, the relative uptake of $Na^+$ in the sediment is lowest, thus the shape of the $Na^+$ profile is most similar to the $Cl^-$ profile, whereas $K^+$ is taken up within the upper 10 m of the sediment column. The $Mg^{2+}$ profiles are characterized by different gradients with a near linear decrease in $Mg^{2+}$ in the upper 11 - 13 m below seafloor (mbsf), whereas with greater sediment depth the gradient becomes less steep. Sulfate concentration decreases nearly linearly from values above 15 mM to values < 1 mM. The SMTZ is reached for all cores at a depth shallower than 6 mbsf. The SMTZ depth is even shallower than 1mbsf for cores GAS-CS07, 08, 13 and 14, which are the cores retrieved on crests. Elevated $CH_4$ concentrations were measured over the entire length of the cores, and in few cases, increased $CH_4$ concentrations were found even above the SMTZ. Regardless of the sample locations, methane is extremely depleted in $^{13}C$, with $\delta^{13}C\text{-}CH_4$ ranging between -62.71 and -72.11 ‰ (Fig.3). The profiles of $NH_4^+$, $PO_4^{3-}$, $SiO_4^{4-}$, $Fe^{2+}$ and $Mn^{2+}$ are very different from one core to another, and values show a large scattering. It has to be noted that the sampling and analytical procedures were not optimized for redox-sensitive species, thus the scatter could be related to procedural artefacts from handling of individual samples. However, this implies that elevated $Fe^{2+}$ and $Mn^{2+}$ concentrations must be considered as lowest estimates, and *in situ* concentrations likely were higher. Nevertheless, clear $Fe^{2+}$ and $Mn^{2+}$ maxima were observed in most of the cores at depths between 8 and 15 mbsf. $NH_4^+$ concentrations reached maximum values in the interval 15 - 22 mbsf, with large differences in absolute $NH_4^+$ concentrations in individual cores.

*Geochemical composition of sediment*

The organic carbon content decreases rapidly from more than 6 to less than 1 wt-% within the upper first meter of the sampled cores (Fig.4). The same rapid decrease is observed for the TIC content, which again increases within the horizon ~2.5 - 4 mbsf, and continues to increase throughout the sampled interval. The sediment shows high and stable contents of Al, Si and Ti along the cores (Fig.5). Na and K contents are low but relatively constant throughout the sediment column. However, Fe and Mn contents, and also Mg and Ca contents, show larger relative differences within each individual core and in between cores. Sediment mineralogical analysis from cores GAS-CS01, CS03, CS07, CS12 and CS14 shows that clay minerals including mica account for 40 to 75 wt-%. This is followed by silicate minerals (feldspar,

plagioclase, and quartz) and carbonate phases (mainly calcite and dolomite). The calcite content remains relatively constant except for few samples collected at the upper part of cores GAS-CS01 and GAS-CS12. The dolomite content is slightly lower than that of calcite and decreases towards the water-sediment interface. Amongst clay minerals, illite is the dominant species and accounts for more than 60% of the total clay mineral fraction (Fig.4). Smectite accounts for 5-20 % of the total clay mineral fraction, and kaolinite and chlorite both usually contribute to less than 10 %. For individual cores, we observe variable trends in clay mineralogy. In GAS-CS01, highest illite (> 90 %) and lowest smectite contents (<10 %) are observed in the narrow interval 4 – 6 mbsf. Below this interval, down to a depth of 22 – 24 mbsf, lower illite (70 %) and higher smectite (20 %) and kaolinite contents (8 %) are found. Below 24 mbsf, this trend is again reversed with higher illite (80 %), and lower smectite (10 %) and kaolinite contents (2 %). In CS01, the chlorite content increases continuously with depth. However, these relations between clay mineralogy and depth cannot easily be transferred to other cores, which clearly indicates differences in lithology and sediment deposition histories between core locations. Mineral data variability is partly reflected in solid phase element profiles. In GAS-CS01, the element composition profile (Fig.5) shows a change in Mg content, which smoothly shift from lower to higher values at a depth of 22 – 24 mbsf. This trend appears to be associated with shifts in Si, Al, K, and Fe contents. Ca contents show considerable variability when comparing different cores, which is not reflected in pore water profiles.

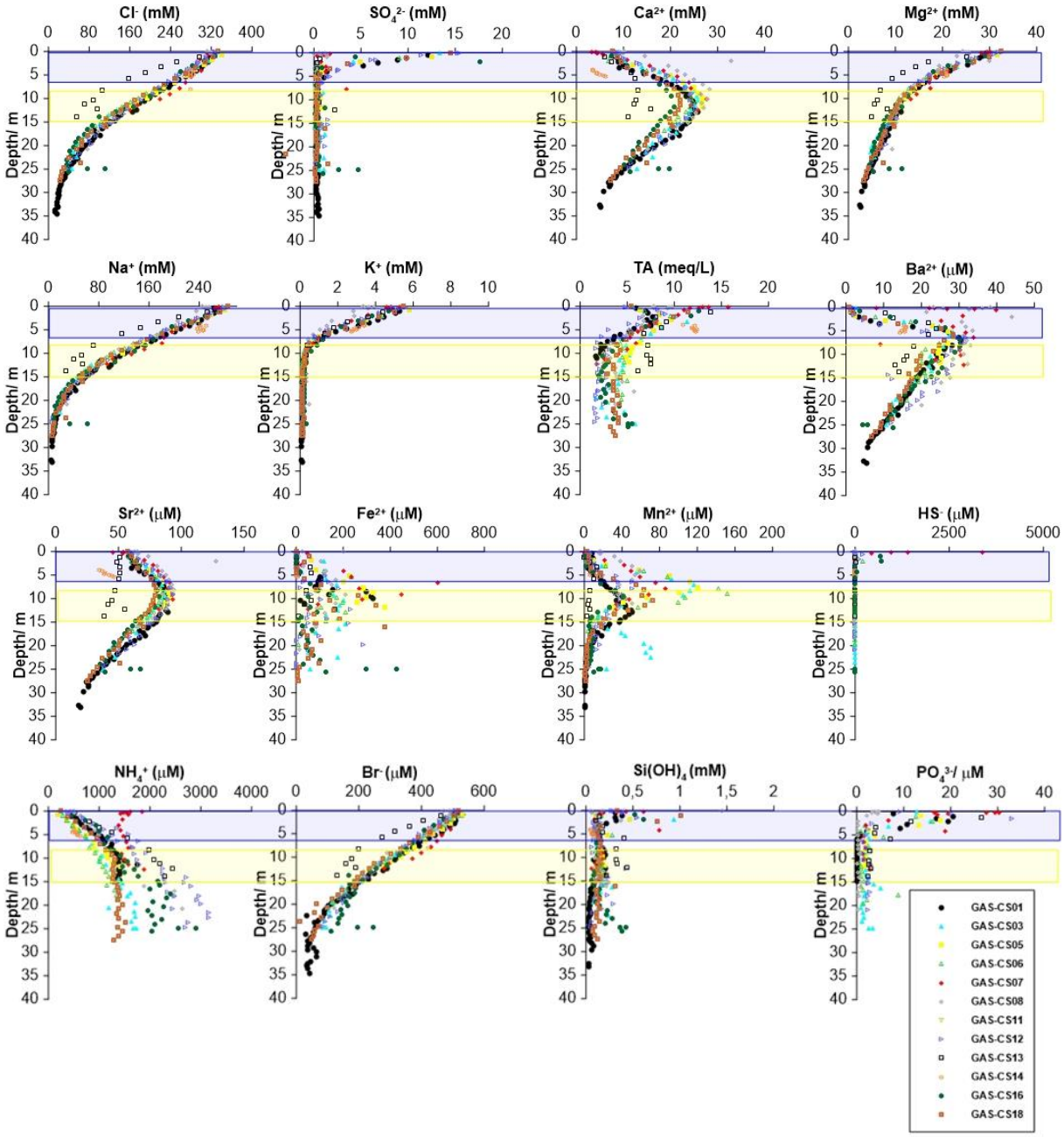


Fig. 2: Pore water depth profiles of dissolved ion concentrations. Grey layer indicates the SMTZ, and yellow layer corresponds to the interval of increased iron concentrations.

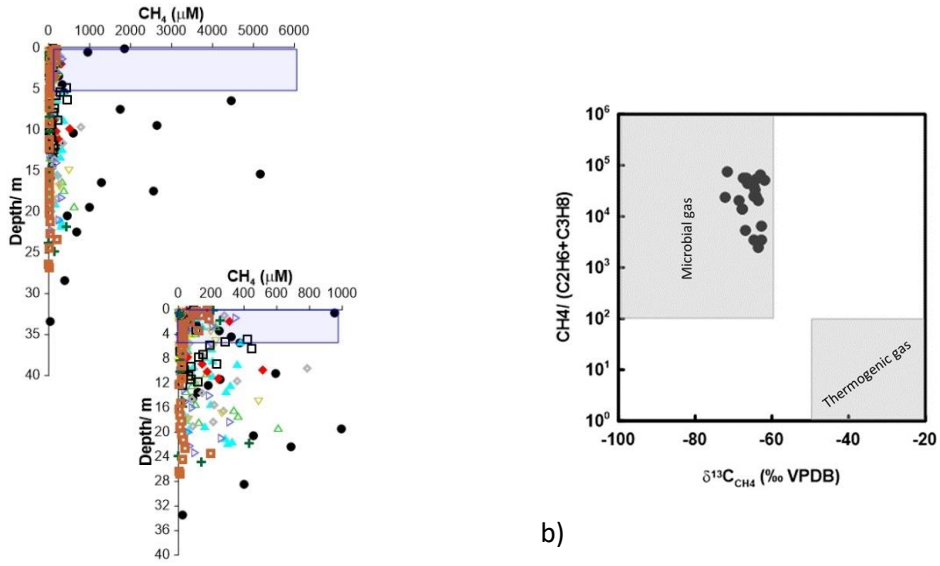


308

309 Fig. 3: a) Pore water depth profiles for dissolved methane concentration, and b) Diagram of $\delta^{13}C$ of methane vs.
310 ethane and propane molecular compositions for the studied venting gases diagram modified after Bernard et al.
311 (Bernard et al., 1978). For the color code of Fig.3a, the reader should refer to Fig.2.

312

313

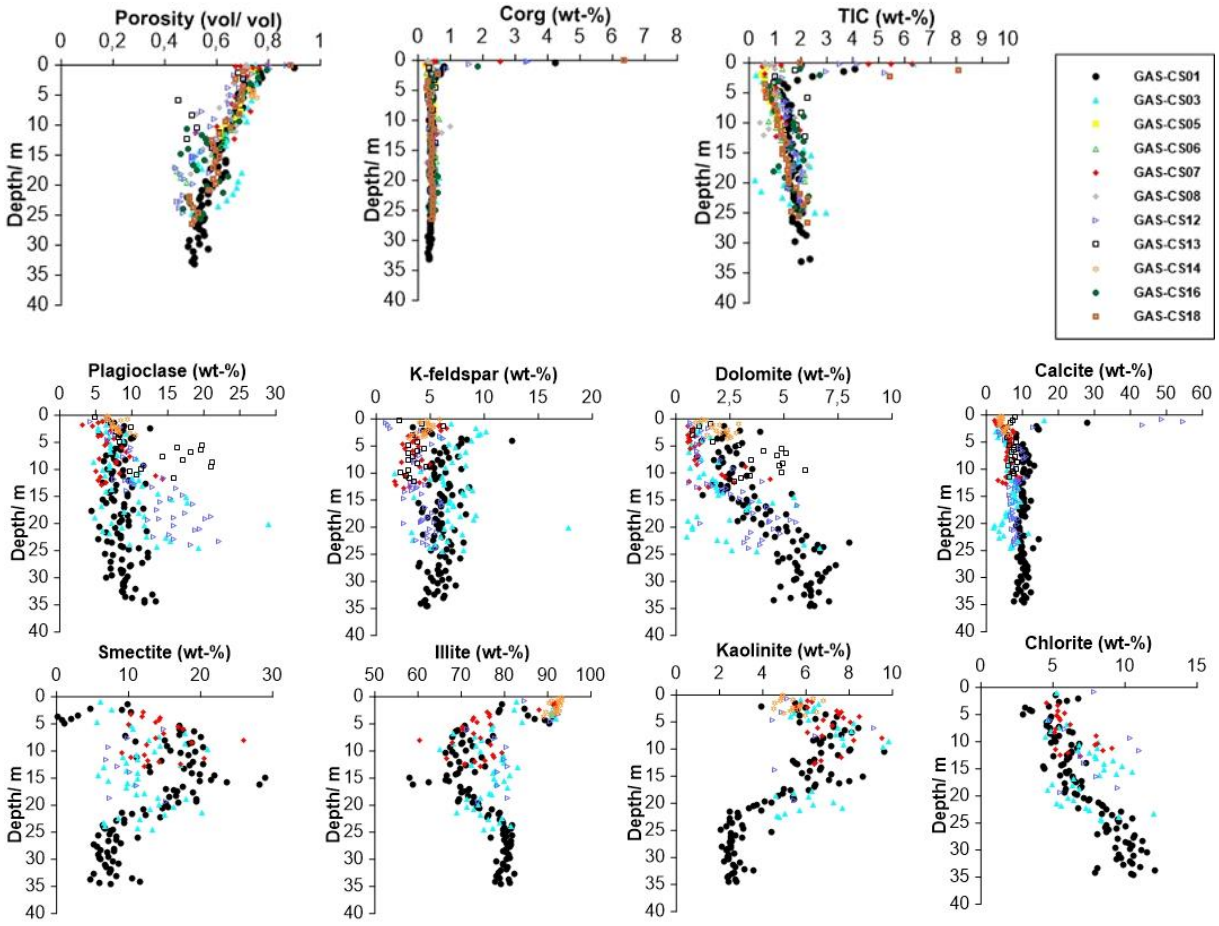


314

315

316 Fig. 4: Solid phase depth profiles of porosity, carbon fractions and mineralogy. Note that the clay fractions were
317 calculated from the total amount of clay only after separation from the other minerals present in the sediment.

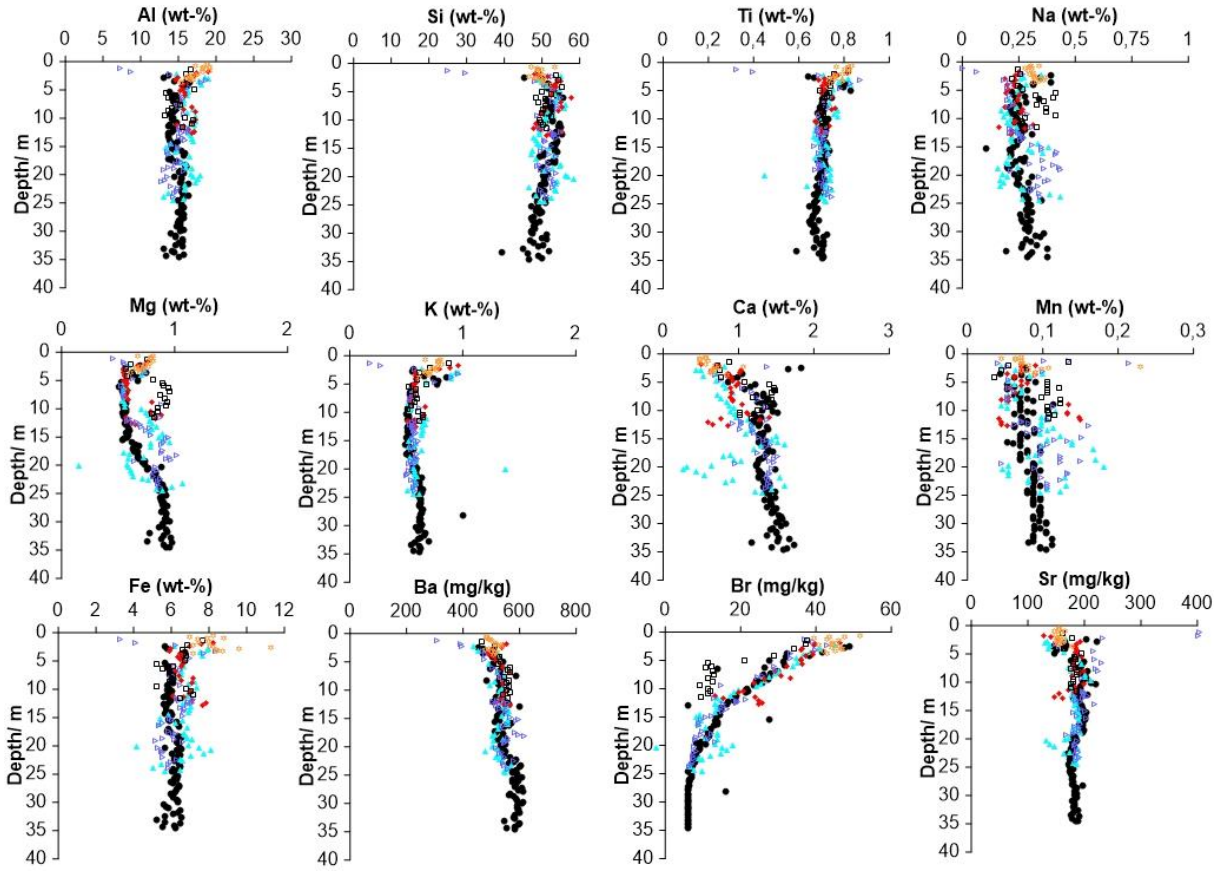


Fig. 5: Solid phase depth profiles of chemical composition (For the color code, the reader should refer to Fig.2)

# Discussion

*Lithology and stratigraphic alignment*

In accordance to known lithological variability, Calypso cores from this study showed substantially different solid phase element and mineral profiles (Figs. 4 & 5). To better distinguish geochemical effects in response to seawater intrusion from lithological changes, we compared specific time windows with known climatic and environmental conditions for four cores from different locations across the northwest Black Sea margin (Fig. 6), GAS-CS01, GAS-CS03, GAS-CS07 and GAS-CS12. A detailed analysis of core GAS-CS01 collected at the shallowest site was recently presented in Martinez-Lamas et al. (2020), with a detailed age model based on the evaluation of chemical, mineralogical and sedimentological markers in comparison with the well-studied core MD04-2790 (Soulet et al., 2011a). The study showed that core GAS-CS01 contains sediments of up to 33 ka BP, belonging to Unit III. The lacustrine-marine (L-M) transition Unit II and the marine Unit I were not clearly identified. However,

337 although it is not well resolved, Unit II was recovered in core GAS-CS12 suggesting the L-M
338 transition at very shallow depth in the first tens of centimeters of cored sediment (Fig. 6).
339 Sedimentary Ca-XRF counts and Ca/Ti ratios, together with the clay mineralogy, allowed the
340 stratigraphic correlation of three additional cores (GAS-CS03, CS07 & CS12) against the well-
341 dated sediment core GAS-CS01 (Fig. 6). The correlations were realized, for example, through
342 the recognition of (i) the Red Layers deposited ca. 17.2-15.7 ka (very low XRF-Ca values;
343 (Soulet et al., 2013; Soulet et al., 2011a)); (ii) Peaks in dolomite content (green bold lines)
344 indicating the influence of the Eastern Alps on the local sedimentation at the MIS 3/2 transition
345 (Martinez-Lamas et al., 2020) and possibly during MIS 4, with potential contribution from low-
346 temperature proto-dolomitization (Liu et al., 2019); (iii) the regional imprint of the Dansgaard/
347 Oeschger (D/O) variability of MIS 3 recognized in the SE Black Sea during ca. 35-60 ka
348 through large variations in the carbonate content (Wegwerth et al., 2015) (Fig. 6). One can
349 clearly see that the cores GAS-CS03 and GAS-CS07 are characterized by a much lower
350 sedimentation rate compared to GAS-CS01 and GAS-CS12. Furthermore, in agreement with
351 previous studies (Soulet et al., 2013; Soulet et al., 2011a), Martinez-Lamas et al. (2020) showed
352 that sediment deposition on the NW Black Sea margin was highly variable at the end of the last
353 glacial period due to the waxing and waning of the AIS and FIS in response to northern
354 hemisphere climate variability. For the time interval prior to the deposition of the red layers
355 during ca. 17.2-15.7 ka BP, hyperpycnal floods from the Danube River were identified as the
356 main sediment source, and sediment deposition and burial of reactive minerals under lacustrine
357 oxic bottom water conditions was much more rapid than modern sedimentation. The analysis
358 of clay mineralogy and Nd isotope signatures of the Danube and its main tributaries suggested
359 that early periods of meltwater release during 32.5-30.5 ka BP supplied smectite-poor, chlorite
360 and dolomite-rich sediments from Eastern Alpine domains (Martinez-Lamas et al., 2020).
361 Thereafter between 30 and 29 ka BP, higher smectite and kaolinite contents suggest that the
362 signals of the sediment contribution from the Danube drainage basin with Dinarides and
363 Carpathians were not overprinted by the Alpine contribution (Martinez-Lamas et al., 2020).
364 Meltwater pulses from the Dniepr basin during the red layer interval supplied illite-rich
365 sediments (Soulet et al., 2013).
366

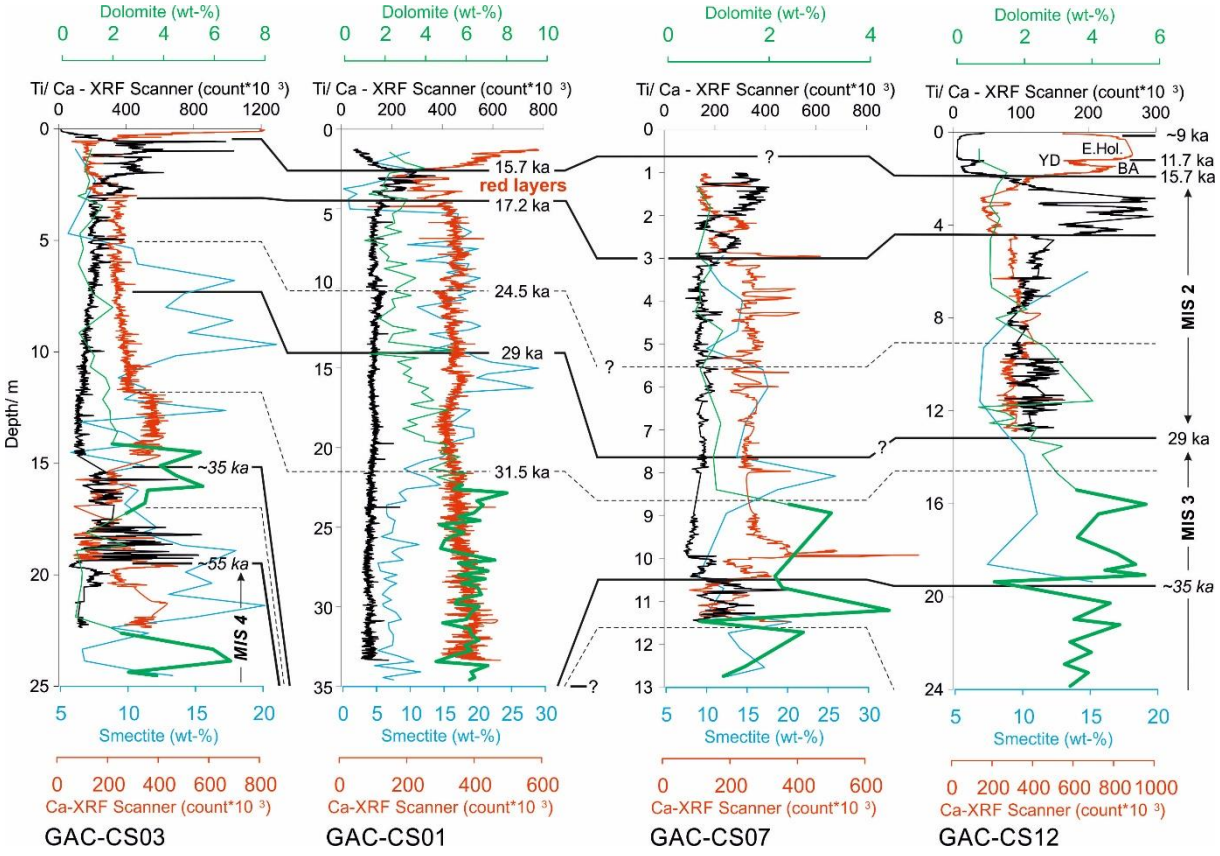


Fig. 6: Age-depth model derived from tentative stratigraphic correlations between cores GAS-CS01 (Martinez-Lamas et al. 2020), GAS-CS03, GAS-CS07 and GAS-CS12 (this study). The upper part of core GAS-CS07 was heavily charged in gas and not reliable for XRF analysis. Ages older that ~33.5 ka (*i.e.* base of GAS-CS01; in italic) are given according to the recognition of stratigraphical features observed in the SE Black Sea (Wegwerth et al., 2015). Peaks in dolomite content (green bold lines) indicate the influence of the Eastern Alps on the local sedimentation (see Martinez-Lamas et al., 2020 for details). All the sedimentary sequences studied here correspond to the lacustrine Unit III of Ross & Degens (1974). BA: Bölling-Alleröd; E.Hol.: Early Holocene; MIS: Marine Isotope Stage; YD: Younger Dryas.

*Transport-reaction characteristics of major ions*

The shape of the pore water profiles illustrates the transport of dissolved species from today's Black Sea marine bottom waters into the lacustrine sediment since the reconnection with the Mediterranean Sea about 9 ka ago (Soulet et al., 2011b). The $Cl^-$-profiles have a slightly concave down shape and show a continuous decrease in salt concentration indicating the transient state of seawater infiltration. Diffusion is the dominant transport process of pore water species at most locations, and clear evidence for disturbances of profiles by recent sediment mass movement through slumping and slope failure events (Hillman et al., 2018b; Riboulot et al., 2017) is not found for most cores. Gas hydrates were recovered throughout core GAS-CS14, therefore the concentrations of dissolved elements might be affected by gas hydrate dissociation

after core recovery. However, a dilution effect is clearly visible only for Ca and Sr in the upper 5 m of sediment, and not for the other dissolved elements. Therefore, hydrate dissolution is not responsible for the low Ca and Sr concentrations. Other processes that we are unable to identify from our dataset might have affected pore water profiles at this location. Core GAS-CS13 also shows characteristically different pore water profiles, especially when comparing with core GAS-CS06, the closest core that is located less than 1 km away. Unlike in core GAS-CS14, there was no evidence for gas hydrates in core GAS-CS13, which was located on an erosional feature (Fig.1). Thus, one possible explanation for the difference of the pore water profiles is that the erosion process has led to loss of surficial sediment, shifting dissolved element concentration to lower values. In principal, upward fluid migration and gas emission could have affected the pore water profiles; however, none of these impacts is obvious from our geochemical data. Another explanation for the difference in pore water profiles from cores GAS-CS13 and GAS-CS06 could be disturbances from the coring operation resulting in the loss of the surficial part. Indeed, the measured chloride concentrations at the uppermost part of all collected cores are lower than the Black Sea bottom water (Bohrmann et al., 2003; Soulet et al., 2010; Zander et al., 2020), and vary between 319 and 339 mM. Core depths have been corrected based on the response of the sensors monitoring the displacement of the piston, which provides a measure of reliability and quality of the coring. However, the loss of the upper sediment cannot be discarded, and comparison with the long piston core studied by Soulet et al. (2010) showed the lowest chloride concentrations of 311, 319 and 297 mM in cores GAS-CS01, GAS-CS08 and GAS-CS13 at ~1.5 mbsf, 2 mbsf, and 3 mbsf, respectively. For our present study, such an additional depth correction due to sediment loss has not been applied, as it does not change the sediment zonation proposed below. Profiles from core GAS-CS16 include two outlying data points at the bottom that likely result from seawater contamination.

The pore water profiles exhibit three intervals where significant changes of element gradients are observed; at 8 - 15 mbsf with distinct maxima of $Ca^{2+}$, $Fe^{2+}$ and $Mn^{2+}$ concentrations, at 22 - 24 mbsf, which coincides with a change of the marine water $Na^{+}$ gradient, and at 31 - 33 mbsf as the current depth of marine $Cl^{-}$ penetration (Fig.2). In this transient-state transport-reaction scenario, $Cl^{-}$ is considered as the most conservative dissolved species. Thus, the change of dissolved element:$Cl^{-}$ ratios indicates the diagenetic release or retention of reactive species (Fig.7). Decreasing $K^{+}$:$Cl^{-}$ and $Mg^{2+}$:$Cl^{-}$ ratios in the upper sediment column (shallower than 11 - 13 mbsf) indicate the uptake of $K^{+}$ and $Mg^{2+}$ by the sediment. $Ca^{2+}$:$Cl^{-}$ and $Sr^{2+}$:$Cl^{-}$ ratios steadily increase with depth, showing the relative enrichment of $Ca^{2+}$ and $Sr^{2+}$ in the pore water. Below the $Ca^{2+}$ maxima (11 -13 mbsf), $Sr^{2+}$:$Ca^{2+}$ and $Mg^{2+}$:$Ca^{2+}$ ratios remain

constant, suggesting a tightly coupled release of $Ca^{2+}$, $Mg^{2+}$ and $Sr^{2+}$. These observations provide evidence for pronounced ion exchange capacities of lacustrine clay minerals, which mainly results in the uptake of $K^+$ and $Mg^{2+}$, and the release of $Ca^{2+}$ and $Sr^{2+}$. Further, the simultaneous release of $Ca^{2+}$ and $Mg^{2+}$ in the deeper sediment column (below 11 - 13 mbsf) indicates dissolution or alteration of silicate and/or carbonate minerals, which could not be constrained in this study.

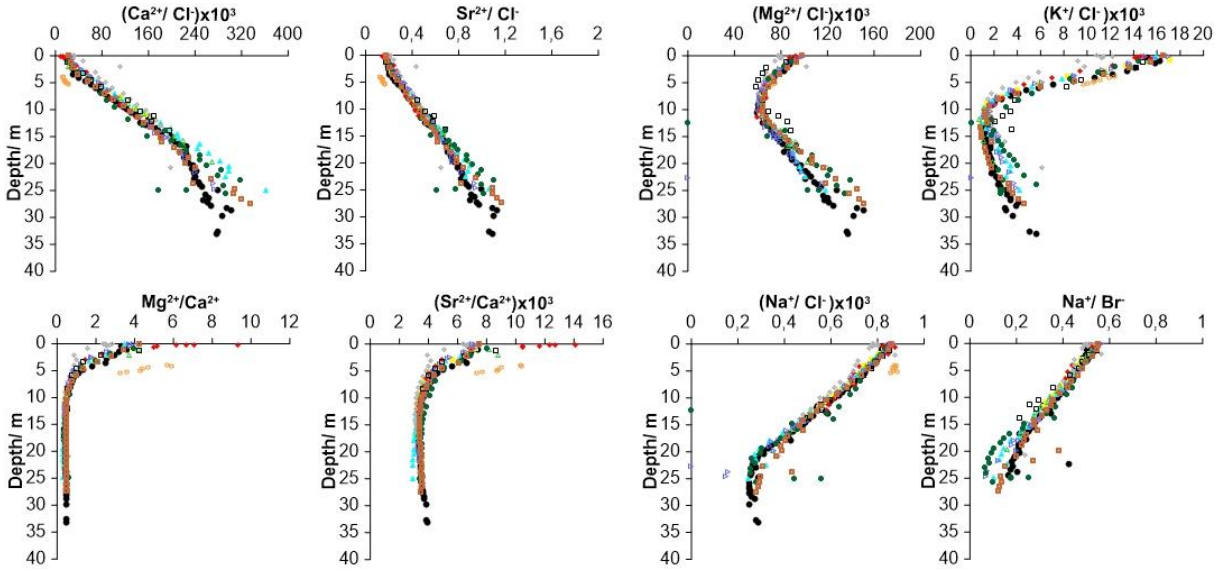


Fig. 7: Ratio of selected pore water species relative to chloride, calcium and bromide (For the color code, the reader should refer to Fig.2)

*Organic matter degradation and terminal electron-accepting processes*

$NH_4^+$ profiles suggest that organic matter degradation and carbon remineralization are more pronounced in the upper 15 mbsf of the cored sediments than below. The organic matter degradation is coupled to organoclastic sulfate reduction (Eq.1).

$$(CH_2O)(NH_3)_{N/C}(H_3PO_4)_{P/C} + 0.5\ SO_4^{2-} \rightarrow 0.5\ HS^- + 0.632\ HCO_3^- + (N/C)\ NH_4^+ + (P/C)\ HPO_4^{2-} + 0.368\ CO_2 + 0.368\ H_2O \quad (1)$$

However, anaerobic oxidation of methane (AOM) largely contributes to sulfate turnover in Black Sea sediments (Eq.2), and defines the depth of the SMTZ (Borowski et al., 1999).

$$CH_4 + SO_4^{2-} \rightarrow HCO_3^- + HS^- + H_2O \quad (2)$$

The correspondence of the depths of $SO_4^{2-}$ depletion and TA maxima suggests a dominant role of sulfate-dependent AOM, which is driven by upward diffusion of microbial methane produced by intense methanogenesis. This observation is corroborated by former studies estimating that AOM accounts for nearly 70% of total $SO_4^{2-}$ turnover in typical Black Sea sediments (Egger et al., 2016; Jorgensen et al., 2001). Closer to methane seeps, AOM becomes even more dominant. The sulfate-depleted sediment below the SMTZ is undersaturated with respect to barite. Therefore, barite undergoes dissolution releasing $Ba^{2+}$ into the pore water in the interval 5-9 mbsf, beneath the AOM interval (Haeckel, 2006; Henkel et al., 2012; Noethen and Kasten, 2011). Very shallow SMTZ depths were determined for cores GAS-CS07, CS08, CS13 and CS14, suggesting enhanced upward methane migration at these sites (Jorgensen et al., 2004; Jorgensen et al., 2001; Zander et al., 2020). This is supported by evidence of both gas hydrates and gas emission at the crests, where these four cores were retrieved. The elevated methane concentrations observed above the SMTZ also indicate enhanced upward $CH_4$ transport or limited AOM efficiency (Knab et al., 2009). Sulfide ($HS^-$) becomes fully depleted below 1 mbsf in all cores although values as high as 3.4 mM were measured at the first meter of sediment (Fig.2), which indicates efficient sulfide removal through iron sulfide precipitation. Usually sedimentary iron acts as the dominant sulfide sink, leading to the accumulation of pyrite and other iron-sulfur minerals (Canfield et al., 1992; Gregory et al., 2019; Jorgensen et al., 2004; Lyons, 1997; Meister et al., 2019; Neretin et al., 2001).

Thus, the transient increase of dissolved $Fe^{2+}$ and $Mn^{2+}$ concentrations below the SMTZ observed in this study (Fig.7) is not clearly related to $HS^-$ profiles as found from previous studies (Jorgensen et al., 2004; Jorgensen et al., 2001; Zander et al., 2020), which indicates high iron and manganese reduction activities and confirms bioavailability of Fe(III) below the SMTZ, similar to recent findings (Egger et al., 2016; Jorgensen et al., 2004; Kraal et al., 2019). The presence of Fe(III) is in accordance with sedimentation characteristics and oxic bottom water conditions during the last glacial, and rapid burial of Fe(III)-bearing minerals may explain the positioning of the deep iron reduction zone. However, it is neither obvious which electron donor is used for deep iron reduction, nor if the positioning of the iron reduction zone is linked to the lacustrine-marine transition or to the presence of a distinct iron pool. Microbial iron reduction was likely an important process prior to seawater inflow under methanogenic conditions, since methanogenesis and iron reduction are largely compatible, and there is evidence that methanogenic organisms can shift metabolic capabilities towards iron reduction in case of iron availability (Bar-Or et al., 2017; Oni et al., 2015; van Bodegom et al., 2004; Vigderovich et al., 2019; Zhang et al., 2012). Thus, the deep iron reduction activity below the

SMTZ strongly suggests iron mobilization from a former refractory iron pool, or a distinct shift in spatial electron donor availability.

POC degradation and methane oxidation could potentially fuel iron reduction at greater depths (Beal et al., 2009; Egger et al., 2017; Egger et al., 2016), and prevent the development of well-constrained reaction zones and distinct iron peaks. However, in most cases high $Fe^{2+}$ concentrations are constrained to particular intervals with distinct maxima, thus Fe(III) reduction appears to be controlled by diffusive transport of reactive species to some extent. Iron reduction could also be driven by DOC degradation. To become available at greater depths, organic compounds must escape from the sulfate reduction zone. DOC supply to greater depths could become possible from an excess availability of DOC compared to sulfate, availability of methane as substrate for sulfate reduction, kinetic limitations of syntrophic substrate transfer, inhibition of sulfate reduction by high sulfide concentrations, or the release of non-competing intermediates, which are not available for microbial sulfate reduction. In principal, the absence of sulfate-reducing microorganisms in lacustrine sediments could explain DOC transport to greater depth, away from the sulfate reduction zone. However, so far there is no evidence for this assumption (Leloup et al., 2007). Clearly, the overall balance (Eq.1) provides very limited mechanistic insight, since sulfate-reducing microorganisms only metabolize small organic molecules (e.g. volatile fatty acids: VFA) or $H_2$, which are products of hydrolytic and fermentative microbial reactions. Thus, organic matter degradation and the concomitant release of DOC close to the sediment-water interface, especially during the high productivity period, could potentially supply substrates for microbial metabolism at greater depths. Whereas seawater intrusion certainly initiated a marked shift of the terminal electron-accepting step to microbial sulfate reduction, it is less clear if and to what extent earlier steps of organic matter degradation have changed, that means, hydrolysis and fermentation.

*Diagenetic reactions in response to seawater intrusion*

Complementary to interval definition from pore water profiles, diagenetic reactions are assigned to 3 specific intervals: (1) AOM and microbial sulfate reduction is located in the interval 0 to 6 mbsf with sulfate depletion to near zero values at the SMTZ, whereas POC is distributed over the upper 15 mbsf. This upper zone is further characterized by silica dissolution leading to $SiO_4^{4-}$ peaks close to the sediment-water interface. (2) Ion exchange processes with lacustrine clay minerals likely control concentrations of major cations in the sediment column above 22-24 mbsf, which results in the net uptake of $K^+$, $Mg^{2+}$ and $Na^+$, and the net release of $Ca^{2+}$ and $Sr^{2+}$ above 11-13 mbsf. (3) In addition to ion exchange reactions, the interval 8-15

514 mbsf shows clear evidence for reverse weathering reactions and dissolution of silicate and/ or
515 carbonate phases, with a net release of $Mg^{2+}$ in a 1:1 ratio with $Ca^{2+}$ in the interval 11-13 mbsf.
516 Further, $Fe^{2+}$ and $Mn^{2+}$ are released between 8-15 mbsf (Fig. 2), which indicates that microbial
517 iron and manganese reduction are linked to these mineral reactions. Since no alkalinity increase
518 is observed below the SMTZ, TA release from mineral weathering or dissolution needs to be
519 balanced by TA consumption. Reverse silicate weathering (Eq.3) could consume TA, alkaline
520 and alkaline earth metals, and release $Ca^{2+}$ (Aloisi et al., 2004a; Kim et al., 2016; Spivack et
521 al., 1987; Vigier et al., 2008). Aluminosilicates such as plagioclase and K-feldspar, which are
522 sufficiently abundant in the sediment, are good candidates for marine reverse weathering
523 reactions such as:
524
525 $$\text{Sr-Ca-Al-Silicate} + SiO_2 + (K^+ + Mg^{2+} + Li^+ + B^{3+}) + HCO_3^- \rightarrow \text{K-Mg-Li-B-Al-Silicate} +$$
526 $$Ca^{2+} + Sr^{2+} + CO_2 + H_2O$$
527 (3)

528 From comparing element budgets over depth from cores GAS-CS01, CS03 and CS07
529 (Fig. 8c, f and i, respectively), it is suggested that the progress of diagenetic processes since the
530 Holocene seawater intrusion is not visible in the sediment element or mineral composition, and
531 the chemical signals could not overprint lithological variability. Budgets from all cores are
532 evaluated as relative changes compared to element contents in the lower parts of GAS-CS01,
533 and unlike pore water profiles, normalized sediment element profiles can be linked to
534 stratigraphical features (see supplementary materials for the core logs).

535 The considerable variability in sediment stratigraphy and mineral composition at different
536 locations does not have a clear effect on reactive transport and pore water profiles of major
537 cations. This could be related to the large pool of reactive minerals or the dominance of kinetic
538 controls of slow geochemical reactions. However, the similarity of pore water profiles could
539 also be linked to microbial metabolism, which would be regulated by substrate availability
540 rather than sediment mineralogy, as discussed above referring to microbial iron reduction.
541 Interestingly, the depletion of seawater cations at 22 - 24 mbsf coincides with changes in clay
542 mineral composition (Fig. 4, GAS-CS01). While these changes appear to be sufficiently
543 explained by variability of sediment sources and input rates during the Late Pleistocene and
544 Holocene, as discussed above, we cannot exclude that ion exchange reactions or other
545 diagenetic processes triggered after seawater intrusion contribute to these conspicuous shifts.
546

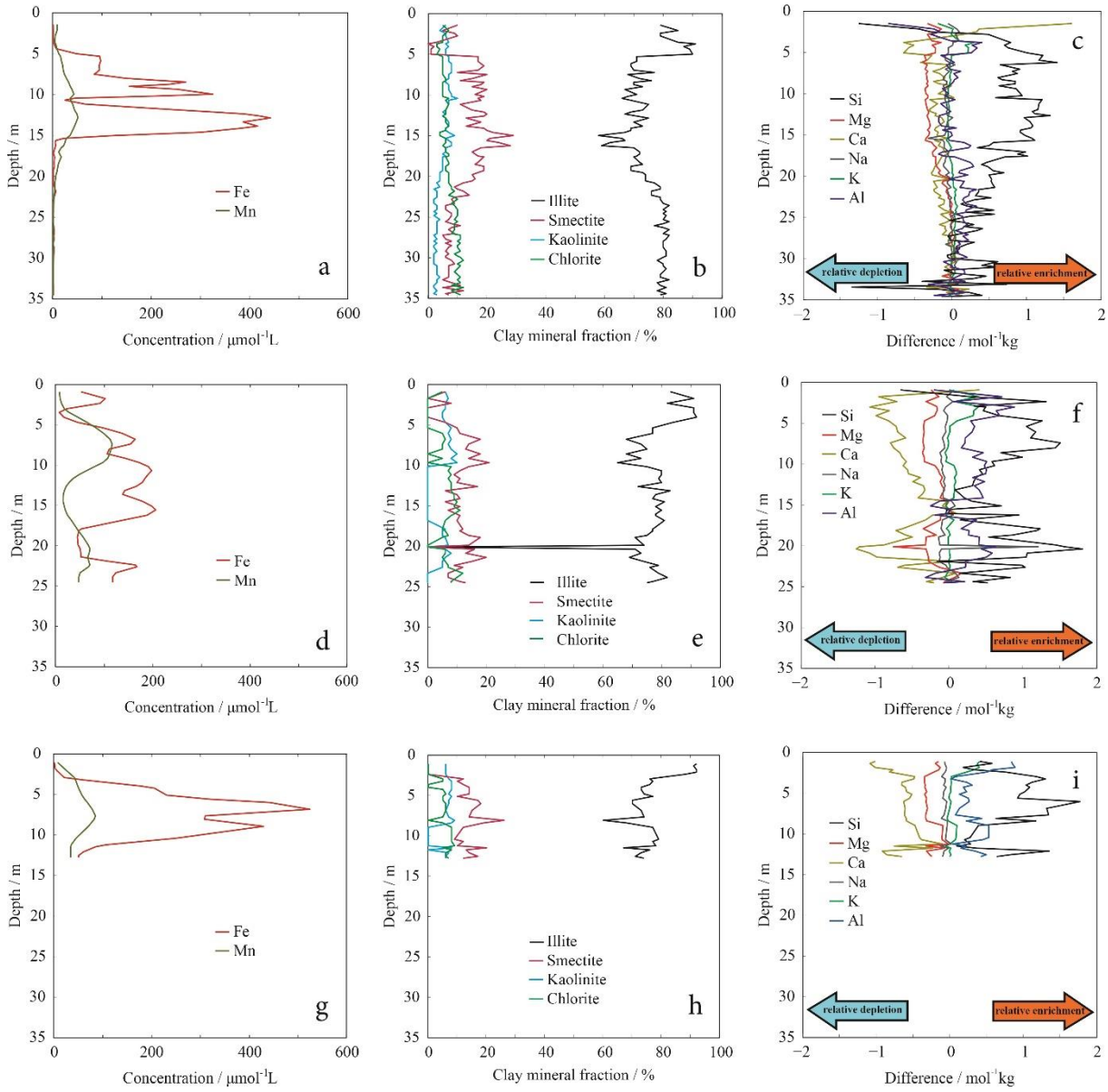


Fig. 8: Dissolved Fe and Mn profiles (a: GAS-CS01, d: GAS-CS03, g: GAS-CS07), clay mineral composition (b: GAS-CS01, e: GAS-CS03, h: GAS-CS07) and sediment composition changes relative to steady state compositions below seawater penetration depth at 31-33 mbsf based on $Cl^-$ profiles in GAS-CS01 (c: GAS-CS01, f: GAS-CS03, i: GAS-CS07).

We hypothesize that the release of $Fe^{2+}$ and $Mn^{2+}$ through microbial iron and manganese reduction was stimulated by the iron and organic substrate availability in response to seawater intrusion. Preliminary X-ray absorption data analyses suggest that iron is strongly associated with phyllosilicates in interval 2, above 22-24 mbsf (Fig.9a). The actual Fe(III) source, however, is not fully resolved. The analysis of Fe(III):Fe(II) ratios shows a trend of increasing Fe(III) content towards shallower sediments depths (Fig.9b), which is counterintuitive to expected increased contents of Fe(II) in the iron reduction zone. However, smectite-bound

Fe(II) is readily oxidized under atmospheric conditions (Rozenson and Heller-Kallai, 1978), which would explain the Fe(III):Fe(II) ratios. Sampling and chemical procedures in this study were not focused on iron analysis, thus redox effects and long-time storage artefacts could influence iron concentration measurements and mineral speciation analysis. Iron speciation analysis further suggests, that at greater depths higher amounts of iron are associated with other minerals (among our reference minerals, goethite, biotite and olivine gave the best results for fitting the deviations from the pure montmorillonite spectrum), and Fe(II) contents were better preserved during storage and analysis.

Since iron at relevant depths is associated with clay minerals rather than with oxy-hydroxide phases, it appears that its reduction could have contributed to clay mineral alteration in a direct or indirect way (Kim et al., 2019; Kostka et al., 2002; Liu et al., 2016; Liu et al., 2017; Pentráková et al., 2013; Vorhies and Gaines, 2009). Thus, clay mineral alteration in the study area could have been influenced by reduction of structurally coordinated Fe(III), which would change charge balances and could trigger changes of the mineral structure or ion exchange capacities (Meunier and El Albani, 2007). Alternatively, if Fe(III) was supplied from an iron oxy-hydroxide phase (e.g. goethite), clay mineral alteration could become driven by equilibration of solid solutions with dissolved $Fe^{2+}$ or dissolution-induced formation of Fe(II)-rich secondary clay minerals.

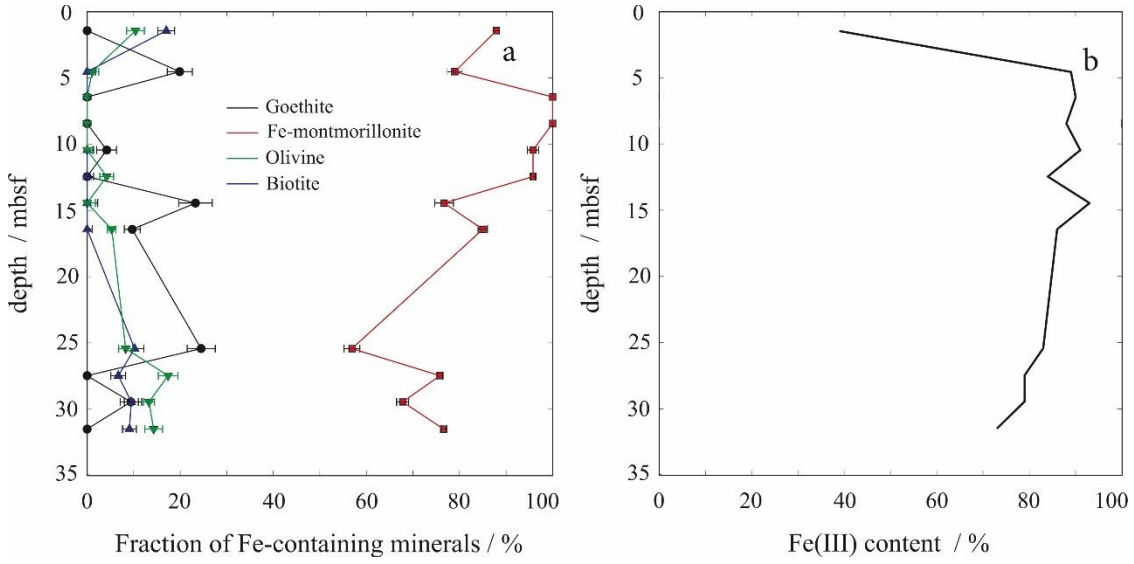


Fig. 9: (a) Solid phase iron speciation and (b) Fe(III) content for core GAS-CS01. Fe(III) content determination by XANES pre-edge fitting is prone to errors and we had not enough suitable reference samples available for a proper calibration of the results. Therefore, absolute values in this graph are uncertain, but relative trends in Fe(III) content are reliable.

585 Summarizing our discussion in a conceptual model (Fig.10), we propose that chemical
586 shifts resulting from seawater intrusion and salt diffusion drive reverse weathering reactions
587 and contribute to the chemical alteration of phyllosilicates. Since iron appears to be largely
588 associated with clay minerals, the alteration of clay minerals could influence iron
589 bioavailability, thus opening up a refractory iron pool. In particular, our conceptual model
590 considers that a redox zonation shift in response to seawater intrusion controls the electron
591 donor supply for microbial iron reduction, acting as the actual driver for iron reduction at depth.
592

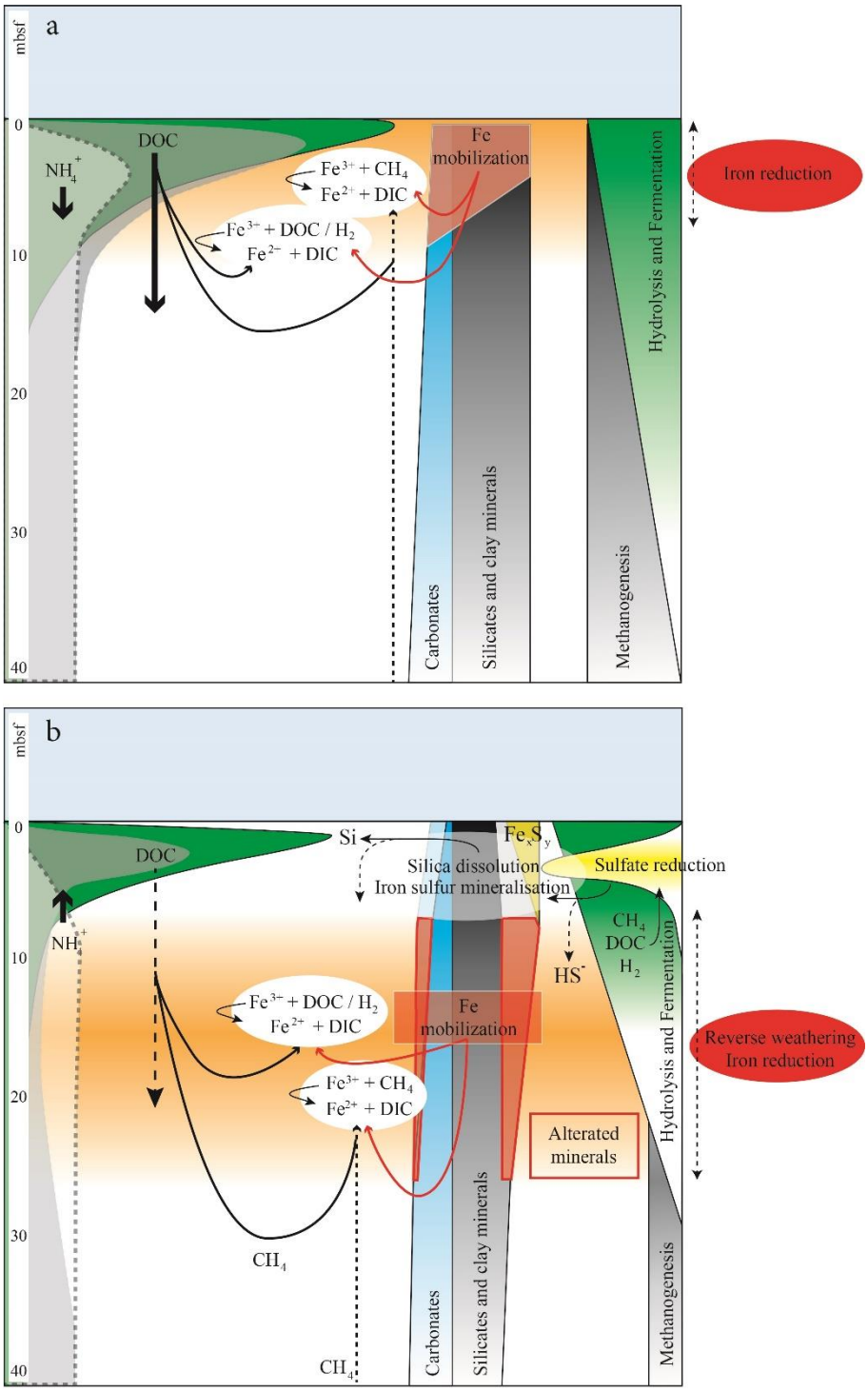


Fig. 10: Conceptual model scheme for coupling of biogeochemical processes and element cycling before (a) and after (b) seawater inflow. Prior to seawater intrusion, methanogenesis and microbial Fe reduction were key processes in Black Sea "lake" sediments. In response to seawater intrusion, ion exchange, dissolution and reverse weathering reactions change the composition of minerals in the lacustrine sediment. In addition to that, the development of a shallow sulfate reduction zone shifts microbial iron reduction to greater depths. We hypothesize that both organoclastic and methanotrophic sulfate reduction contribute to the overall sulfate turnover, and that, however, the organic carbon turnover has not become fully adapted to sulfate reduction under transient state

conditions. Thus, dissolved organic compounds (i.e. DOC) escape from the sulfate reduction zone and fuel microbial iron reduction at depth.

## Conclusion

Pore water data show the progress of reactive-transport processes in lacustrine sediments at the Black Sea western slope after seawater intrusion into the basin 9 ka BP. Intense sulfate reduction and cation exchange at shallow depths provide clear evidence of ongoing dynamic alteration of the lacustrine sediments. The seawater intrusion drives the release of $Ca^{2+}$ and $Sr^{2+}$, and the uptake of $K^{+}$, $Mg^{2+}$ and Na+ in the sediment through reverse weathering and ion exchange, and affects clay mineral pools and iron bioavailability below the SMTZ. Post-depositional disturbances are not clearly visible, and strong sediment and pore water evidence for mass movement events and slope destabilization is lacking. Similarly, the intense gas seepage, which guided the choice of coring locations, was not significantly reflected in pore water profiles, except for a shoaling of the SMTZ. However, the large variability of sediment composition and mineralogy, which results from highly dynamic changes in solids transport and deposition rates during the last glacial period and Holocene, strongly complicates the geochemical interpretations.

**Acknowledgements**

We thank the captain and his crew on-board the *RV Pourquoi pas?* crew for their technical support and advices. Financial support for the cruise was provided by Ifremer and the European project Midas (grant agreement 603418). This work is also a contribution to the BLAME project sponsored by the French National Research Agency (ANR-18-CE01-0007) and the SUGAR project funded by the German Federal Ministry of Economic Affairs and Energy (grant no. 03SX320A) and the German Federal Ministry of Education and Research (grant nos. 03G0819A and 03G0856A). We acknowledge DESY (Hamburg, Germany), a member of the Helmholtz Association HGF, for the provision of experimental facilities. Parts of this research were carried out at beamline P64 and we would like to thank Wolfgang A. Caliebe (DESY) for assistance in operating the beamline and Anna-Kathrin Retschko (GEOMAR) for sample preparation. We thank Andrea Bodenbinder, Bettina Domeyer, Anke Bleyer and Regina Surberg for the excellent support with shore-based analyses, as well as Dr. Guillaume Soulet for constructive discussion. We also thank two anonymous reviewers for their valuable comments, which significantly improved the content of the paper.

## Reference


Aloisi, G., Drews, M., Wallmann, K., Bohrmann, G., 2004a. Fluid expulsion from the Dvurechenskii mud volcano (Black Sea): Part I. Fluid sources and relevance to Li, B, Sr, I and dissolved inorganic nitrogen cycles. Earth and Planetary Science Letters 225, 347-363.

Aloisi, G., Wallmann, K., Drews, M., 2004b. Evidence for the submarine weathering of silicate minerals in Black Sea sediments: Possible implications for the marine Li and B cycles. Geochemistry Geophysics Geosystems 5.

Ballas, G., Garziglia, S., Sultan, N., Pelleter, E., Toucanne, S., Marsset, T., Riboulot, V., Ker, S., 2018. Influence of early diagenesis on geotechnical properties of clay sediments (Romania, Black Sea). Engineering Geology 240, 175-188.

Bar-Or, I., Elvert, M., Eckert, W., Kushmaro, A., Vigderovich, H., Zhu, Q., Ben-Dov, E., Sivan, O., 2017. Iron-coupled anaerobic oxidation of methane performed by a mixed bacterial-archaeal community based on poorly reactive minerals. Environmental science & technology 51, 12293-12301.

Beal, E.J., House, C.H., Orphan, V.J., 2009. Manganese-and iron-dependent marine methane oxidation. Science 325, 184-187.

Bernard, B.B., Brooks, J.M., Sackett, W.M., 1978. Light-hydrocarbons in recent texas continental-shelf and slope sediments. Journal of Geophysical Research-Oceans and Atmospheres 83, 4053-4061.

Bialas, J., Klaucke, I., Haeckel, M., 2014. FS MARIA S. MERIAN Fahrtbericht / Cruise Report MSM34/1 & 2 - SUGAR Site ; Varna – Varna, 06.12.13 – 16.01.14. GEOMAR Report N. Ser. 015. GEOMAR Helmholtz-Zentrum für Ozeanforschung, Kiel, Germany, Open Access, DOI 10.3289/GEOMAR_REP_NS_15_2014, 111 pp.

Blinova, V.N., Ivanov, M.K., Bohrmann, G., 2003. Hydrocarbon gases in deposits from mud volcanoes in the Sorokin Trough, north-eastern Black Sea. Geo-Marine Letters 23, 250-257.

Bohrmann, G., Ivanov, M., Foucher, J.P., Spiess, V., Bialas, J., Greinert, J., Weinrebe, W., Abegg, F., Aloisi, G., Artemov, Y., Blinova, V., Drews, M., Heidersdorf, F., Krabbenhoft, A., Klaucke, I., Krastel, S., Leder, T., Polikarpov, I., Saburova, M., Schmale, O., Seifert, R., Volkonskaya, A., Zillmer, M., 2003. Mud volcanoes and gas hydrates in the Black Sea: new data from Dvurechenskii and Odessa mud volcanoes. Geo-Marine Letters 23, 239-249.

Borowski, W.S., Paull, C.K., Ussler, W., 1999. Global and local variations of interstitial sulfate gradients in deep-water, continental margin sediments: Sensitivity to underlying methane and gas hydrates. Marine Geology 159, 131-154.

Caliebe, W.A., Murzin, V., Kalinko, A., Görlitz, M., 2019. High-flux XAFS-beamline P64 at PETRA III, AIP Conference Proceedings. AIP Publishing, p. 060031.

Calvin, S., 2013. XAFS for Everyone. CRC press.

Canfield, D.E., Raiswell, R., Bottrell, S., 1992. The reactivity of sedimentary iron minerals toward sulfide. American Journal of Science 292, 659-683.

Constantinescu, A.M., Toucanne, S., Dennielou, B., Jorry, S.J., Mulder, T., Lericolais, G., 2015. Evolution of the Danube Deep-Sea Fan since the Last Glacial Maximum: new insights into Black Sea water-level fluctuations. Marine Geology 367, 50-68.

Egger, M., Hagens, M., Sapart, C.J., Dijkstra, N., van Helmond, N., Mogollon, J.M., Risgaard-Petersen, N., van der Veen, C., Kasten, S., Riedinger, N., Bottcher, M.E., Rockmann, T., Jorgensen, B.B., Slomp, C.P., 2017. Iron oxide reduction in methane-rich deep Baltic Sea sediments. Geochimica Et Cosmochimica Acta 207, 256-276.

Egger, M., Kraal, P., Jilbert, T., Sulu-Gambari, F., Sapart, C.J., Rockmann, T., Slomp, C.P., 2016. Anaerobic oxidation of methane alters sediment records of sulfur, iron and phosphorus in the Black Sea. Biogeosciences 13, 5333-5355.

Grasshoff, K., Kremling, K., Ehrhardt, M., 1999. Methods of seawater analysis, Wiley VCH. Weinheim, Germany.

Gregory, D., Mukherjee, I., Olson, S.L., Large, R.R., Danyushevsky, L.V., Stepanov, A.S., Avila, J.N., Cliff, J., Ireland, T.R., Raiswell, R., Olin, P.H., Maslennikov, V.V., Lyons, T.W., 2019. The formation

686 mechanisms of sedimentary pyrite nodules determined by trace element and sulfur isotope
687 microanalysis. Geochimica et Cosmochimica Acta 259, 53-68.
688 Greinert, J., Artemov, Y., Egorov, V., De Batist, M., McGinnis, D., 2006. 1300-m-high rising bubbles from
689 mud volcanoes at 2080m in the Black Sea: Hydroacoustic characteristics and temporal variability. Earth
690 and Planetary Science Letters 244, 1-15.
691 Greinert, J., McGinnis, D.F., Naudts, L., Linke, P., De Batist, M., 2010. Atmospheric methane flux from
692 bubbling seeps: Spatially extrapolated quantification from a Black Sea shelf area. Journal of
693 Geophysical Research-Oceans 115.
694 Haeckel, M., 2006. A transport-reaction model of the hydrological systems of the Costa Rica subduction
695 zone, Proceedings of the Ocean Drilling Program, Scientific Results, Leg, pp. 1-26.
696 Haeckel, M., Bialas, J., Klaucke, I., Wallmann, K., Bohrmann, G., Schwalenberg, K., 2015. Gas hydrate
697 occurrences in the Black Sea–new observations from the German SUGAR project. Fire in the Ice:
698 Methane Hydrate Newsletter 15, 6-9.
699 Haffert, L., Haeckel, M., Liebetrau, V., Berndt, C., Hensen, C., Nuzzo, M., Reitz, A., Scholz, F., Schonfeld,
700 J., Perez-Garcia, C., Weise, S.M., 2013. Fluid evolution and authigenic mineral paragenesis related to
701 salt diapirism - The Mercator mud volcano in the Gulf of Cadiz. Geochimica Et Cosmochimica Acta 106,
702 261-286.
703 Heeschen, K.U., Haeckel, M., Klaucke, I., Ivanov, M.K., Bohrmann, G., 2011. Quantifying in-situ gas
704 hydrates at active seep sites in the eastern Black Sea using pressure coring technique. Biogeosciences
705 8, 3555-3565.
706 Henkel, S., Mogollon, J.M., Noethen, K., Franke, C., Bogus, K., Robin, E., Bahr, A., Blumenberg, M., Pape,
707 T., Seifert, R., Maerz, C., de Lange, G.J., Kasten, S., 2012. Diagenetic barium cycling in Black Sea
708 sediments - A case study for anoxic marine environments. Geochimica et Cosmochimica Acta 88, 88-
709 105.
710 Hillman, J.I.T., Klaucke, I., Bialas, J., Feldman, H., Drexler, T., Awwiller, D., Atgin, O., Cifci, G., Badhani,
711 S., 2018a. Gas migration pathways and slope failures in the Danube Fan, Black Sea. Marine and
712 Petroleum Geology 92, 1069-1084.
713 Hillman, J.I.T., Klaucke, I., Bialas, J., Feldman, H., Drexler, T., Awwiller, D., Atgin, O., Çifçi, G., Badhani,
714 S., 2018b. Gas migration pathways and slope failures in the Danube Fan, Black Sea. Marine and
715 Petroleum Geology 92, 1069-1084.
716 Holmkvist, L., Kamyshny, A., Jr., Vogt, C., Vamvakopoulos, K., Ferdelman, T.G., Jorgensen, B.B., 2011.
717 Sulfate reduction below the sulfate-methane transition in Black Sea sediments. Deep-Sea Research
718 Part I-Oceanographic Research Papers 58, 493-504.
719 Holtzappel, T., 1985. Les minéraux argileux, préparation, analyse diffractométrique et détermination.
720 Société Géologique du nord 12, 1-36.
721 Huvaj, Y.N., Huff, W.D., 2016. Clay mineralogy and geochemistry of three offshore wells in the
722 southwestern Black Sea, northern Turkey: the effect of burial diagenesis on the conversion of smectite
723 to illite. Turkish Journal of Earth Sciences 25, 592-610.
724 Jorgensen, B.B., Böttcher, M.E., Lüschen, H., Neretin, L.N., Volkov, I.I., 2004. Anaerobic methane
725 oxidation and a deep H2S sink generate isotopically heavy sulfides in Black Sea sediments. Geochimica
726 et Cosmochimica Acta 68, 2095-2118.
727 Jorgensen, B.B., Weber, A., Zopfi, J., 2001. Sulfate reduction and anaerobic methane oxidation in Black
728 Sea sediments. Deep-Sea Research Part I-Oceanographic Research Papers 48, 2097-2120.
729 Ker, S., Thomas, Y., Riboulot, V., Sultan, N., Bernard, C., Scalabrin, C., Ion, G., Marsset, B., 2019.
730 Anomalously Deep BSR Related to a Transient State of the Gas Hydrate System in the Western Black
731 Sea. Geochemistry Geophysics Geosystems 20, 442-459.
732 Kessler, J.D., Reeburgh, W.S., Southon, J., Seifert, R., Michaelis, W., Tyler, S.C., 2006a. Basin-wide
733 estimates of the input of methane from seeps and clathrates to the Black Sea. Earth and Planetary
734 Science Letters 243, 366-375.
735 Kessler, J.D., Reeburgh, W.S., Tyler, S.C., 2006b. Controls on methane concentration and stable isotope
736 (delta H-2-CH4 and delta C-13-CH4) distributions in the water columns of the Black Sea and Cariaco
737 Basin. Global biogeochemical cycles 20.

738 Kim, J., Dong, H., Yang, K., Park, H., Elliott, W.C., Spivack, A., Koo, T., Kim, G., Morono, Y., Henkel, S.,
739 Inagaki, F., Zeng, Q., Hoshino, T., Heuer, V.B., 2019. Naturally occurring, microbially induced smectite-
740 to-illite reaction. Geology 47, 535-539.
741 Kim, J.H., Torres, M.E., Haley, B.A., Ryu, J.S., Park, M.H., Hong, W.L., Choi, J., 2016. Marine silicate
742 weathering in the anoxic sediment of the Ulleung Basin: Evidence and consequences. Geochemistry
743 Geophysics Geosystems 17, 3437-3453.
744 Knab, N.J., Cragg, B.A., Hornibrook, E.R.C., Holmkvist, L., Pancost, R.D., Borowski, C., Parkes, R.J.,
745 JÃ¸rgensen, B.B., 2009. Regulation of anaerobic methane oxidation in sediments of the black sea.
746 Biogeosciences 6, 1505-1518.
747 Kosarev, A.N., 2007. The Black Sea Environment. Springer.
748 Kostka, J.E., Dalton, D.D., Skelton, H., Dollhopf, S., Stucki, J.W., 2002. Growth of iron (III)-reducing
749 bacteria on clay minerals as the sole electron acceptor and comparison of growth yields on a variety
750 of oxidized iron forms. Appl. Environ. Microbiol. 68, 6256-6262.
751 Kraal, P., Yucel, M., Slomp, C.P., 2019. Turbidite deposition and diagenesis in the southwestern Black
752 Sea: Implications for biogeochemical cycling in an anoxic basin. Marine Chemistry 209, 48-61.
753 Leloup, J., Loy, A., Knab, N.J., Borowski, C., Wagner, M., Jørgensen, B.B., 2007. Diversity and abundance
754 of sulfate-reducing microorganisms in the sulfate and methane zones of a marine sediment, Black Sea.
755 Environmental microbiology 9, 131-142.
756 Lericolais, G., Bourget, J., Popescu, I., Jermannaud, P., Mulder, T., Jorry, S., Panin, N., 2013. Late
757 Quaternary deep-sea sedimentation in the western Black Sea: New insights from recent coring and
758 seismic data in the deep basin. Global and Planetary Change 103, 232-247.
759 Liu, D., Wang, F., Dong, H., Wang, H., Zhao, L., Huang, L., Wu, L., 2016. Biological reduction of structural
760 Fe(III) in smectites by a marine bacterium at 0.1 and 20 MPa. Chemical Geology 438, 1-10.
761 Liu, D., Xu, Y., Papineau, D., Yu, N., Fan, Q., Qiu, X., Wang, H., 2019. Experimental evidence for abiotic
762 formation of low-temperature proto-dolomite facilitated by clay minerals. Geochimica et
763 Cosmochimica Acta 247, 83-95.
764 Liu, G., Qiu, S., Liu, B., Pu, Y., Gao, Z., Wang, J., Jin, R., Zhou, J., 2017. Microbial reduction of Fe(III)-
765 bearing clay minerals in the presence of humic acids. Scientific Reports 7.
766 Lyons, T.W., 1997. Sulfur isotopic trends and pathways of iron sulfide formation in upper Holocene
767 sediments of the anoxic Black Sea. Geochimica Et Cosmochimica Acta 61, 3367-3382.
768 Major, C.O., Goldstein, S.L., Ryan, W.B.F., Lericolais, G., Piotrowski, A.M., Hajdas, I., 2006. The co-
769 evolution of Black Sea level and composition through the last deglaciation and its paleoclimatic
770 significance. Quaternary Science Reviews 25, 2031-2047.
771 Martinez-Lamas, R., Toucanne, S., Debret, M., Riboulot, V., Deloffre, J., Boissier, A., Cheron, S., Pitel,
772 M., Bayon, G., Giosan, L., 2020. Linking Danube River activity to Alpine Ice-Sheet fluctuations during
773 the last glacial (ca. 33–17 ka BP): Insights into the continental signature of Heinrich Stadials.
774 Quaternary Science Reviews 229, 106136.
775 Meister, P., Brunner, B., Picard, A., Böttcher, M.E., Jørgensen, B.B., 2019. Sulphur and carbon isotopes
776 as tracers of past sub-seafloor microbial activity. Scientific reports 9, 1-9.
777 Meister, P., Liu, B., Ferdelman, T.G., Jørgensen, B.B., Khalili, A., 2013. Control of sulphate and methane
778 distributions in marine sediments by organic matter reactivity. Geochimica et Cosmochimica Acta 104,
779 183-193.
780 Meunier, A., El Albani, A., 2007. The glauconite-Fe-illite-Fe-smectite problem: A critical review. Terra
781 Nova 19, 95-104.
782 Naudts, L., Greinert, J., Artemov, Y., Staelens, P., Poort, J., Van Rensbergen, P., De Batist, M., 2006.
783 Geological and morphological setting of 2778 methane seeps in the Dnepr paleo-delta, northwestern
784 Black Sea. Marine Geology 227, 177-199.
785 Neretin, L.N., Volkov, I.I., Böttcher, M.E., Grinenko, V.A., 2001. A sulfur budget for the Black Sea anoxic
786 zone. Deep Sea Research Part I: Oceanographic Research Papers 48, 2569-2593.
787 Niewohner, C., Hensen, C., Kasten, S., Zabel, M., Schulz, H.D., 1998. Deep sulfate reduction completely
788 mediated by anaerobic methane oxidation in sediments of the upwelling area off Namibia. Geochimica
789 et Cosmochimica Acta 62, 455-464.

790 Noethen, K., Kasten, S., 2011. Reconstructing changes in seep activity by means of pore water and solid
791 phase Sr/Ca and Mg/Ca ratios in pockmark sediments of the Northern Congo Fan. Marine Geology 287,
792 1-13.
793 Oni, O., Miyatake, T., Kasten, S., Richter-Heitmann, T., Fischer, D., Wagenknecht, L., Kulkarni, A.,
794 Blumers, M., Shylin, S.I., Ksenofontov, V., Costa, B.F.O., Klingelhofer, G., Friedrich, M.W., 2015. Distinct
795 microbial populations are tightly linked to the profile of dissolved iron in the methanic sediments of
796 the Helgoland mud area, North Sea. Frontiers in Microbiology 6.
797 Özsoy, E., Ünlüata, Ü., 1997. Oceanography of the Black Sea: a review of some recent results. Earth-
798 Science Reviews 42, 231-272.
799 Pape, T., Blumenberg, M., Seifert, R., Bohrmann, G., Michaelis, W., 2008. Marine Methane
800 Biogeochemistry of the Black Sea: A Review, in: Dilek, Y.F.H.M.K. (Ed.), Links between Geological
801 Processes, Microbial Activities & Evolution of Life: Microbes and Geology, pp. 281-311.
802 Pentráková, L., Su, K., Pentrák, M., Stucki, J., 2013. A review of microbial redox interactions with
803 structural Fe in clay minerals. Clay Minerals 48, 543-560.
804 Piper, D.Z., Calvert, S., 2011. Holocene and late glacial palaeoceanography and palaeolimnology of the
805 Black Sea: changing sediment provenance and basin hydrography over the past 20,000 years.
806 Geochimica et Cosmochimica Acta 75, 5597-5624.
807 Popescu, I., De Batist, M., Lericolais, G., Nouze, H., Poort, J., Panin, N., Versteeg, W., Gillet, H., 2006.
808 Multiple bottom-simulating reflections in the Black Sea: Potential proxies of past climate conditions.
809 Marine Geology 227, 163-176.
810 Popescu, I., Lericolais, G., Panin, N., De Batist, M., Gillet, H., 2007. Seismic expression of gas and gas
811 hydrates across the western Black Sea. Geo-Marine Letters 27, 173-183.
812 Popescu, I., Lericolais, G., Panin, N., Normand, A., Dinu, C., Le Drezen, E., 2004. The Danube submarine
813 canyon (Black Sea): morphology and sedimentary processes. Marine Geology 206, 249-265.
814 Ravel, B., Newville, M., 2005. ATHENA, ARTEMIS, HEPHAESTUS: data analysis for X-ray absorption
815 spectroscopy using IFEFFIT. Journal of synchrotron radiation 12, 537-541.
816 Reeburgh, W.S., 2007. Oceanic methane biogeochemistry. Chemical Reviews 107, 486-513.
817 Reeburgh, W.S., Ward, B.B., Whalen, S.C., Sandbeck, K.A., Kilpatrick, K.A., Kerkhof, L.J., 1991. Black-sea
818 methane geochemistry. Deep-Sea Research Part a-Oceanographic Research Papers 38, S1189-S1210.
819 Regnier, P., Dale, A.W., Arndt, S., LaRowe, D., Mogollon, J., Van Cappellen, P., 2011. Quantitative
820 analysis of anaerobic oxidation of methane (AOM) in marine sediments: A modeling perspective. Earth-
821 Science Reviews.
822 Reitz, A., Pape, T., Haeckel, M., Schmidt, M., Berner, U., Scholz, F., Liebetrau, V., Aloisi, G., Weise, S.M.,
823 Wallmann, K., 2011. Sources of fluids and gases expelled at cold seeps offshore Georgia, eastern Black
824 Sea. Geochimica et Cosmochimica Acta 75, 3250-3268.
825 Riboulot, V., Cattaneo, A., Scalabrin, C., Gaillot, A., Jouet, G., Ballas, G., Marsset, T., Garziglia, S., Ker,
826 S., 2017. Control of the geomorphology and gas hydrate extent on widespread gas emissions offshore
827 Romania. Bulletin De La Societe Geologique De France 188.
828 Riboulot, V., Ker, S., Sultan, N., Thomas, Y., Marsset, B., Scalabrin, C., Ruffine, L., Boulart, C., Ion, G.,
829 2018. Freshwater lake to salt-water sea causing widespread hydrate dissociation in the Black Sea.
830 Nature Communications 9.
831 Robinson, A., Rudat, J., Banks, C., Wiles, R., 1996. Petroleum geology of the Black Sea. Marine and
832 Petroleum Geology 13, 195-223.
833 Robinson, A.G., 1997. Regional and Petroleum Geology of the Black Sea and Surrounding Region: AAPG
834 Memoir 68. AAPG.
835 Roemer, M., Sahling, H., Pape, T., Bahr, A., Feseker, T., Wintersteller, P., Bohrmann, G., 2012.
836 Geological control and magnitude of methane ebullition from a high-flux seep area in the Black Sea-
837 the Kerch seep area. Marine Geology 319, 57-74.
838 Rozenson, I., Heller-Kallai, L., 1978. Reduction and oxidation of Fe 3+ in dioctahedral smectites—III.
839 Oxidation of octahedral iron in montmorillonite. Clays and Clay Minerals 26, 88-92.

Schmale, O., Beaubien, S.E., Rehder, G., Greinert, J., Lombardi, S., 2010a. Gas seepage in the Dnepr paleo-delta area (NW-Black Sea) and its regional impact on the water column methane cycle. Journal of Marine Systems 80, 90-100.
Schmale, O., Greinert, J., Rehder, G., 2005. Methane emission from high-intensity marine gas seeps in the Black Sea into the atmosphere. Geophysical Research Letters 32.
Schmale, O., Haeckel, M., McGinnis, D.F., 2011. Response of the Black Sea methane budget to massive short-term submarine inputs of methane. Biogeosciences 8, 911-918.
Schmale, O., von Deimling, J.S., Gulzow, W., Nausch, G., Waniek, J.J., Rehder, G., 2010b. Distribution of methane in the water column of the Baltic Sea. Geophysical Research Letters 37.
Scholz, F., Löscher, C.R., Fiskal, A., Sommer, S., Hensen, C., Lomnitz, U., Wuttig, K., Göttlicher, J., Kossel, E., Steininger, R., 2016. Nitrate-dependent iron oxidation limits iron transport in anoxic ocean regions. Earth and Planetary Science Letters 454, 272-281.
Schouten, S., Wakeham, S.G., Damsté, J.S.S., 2001. Evidence for anaerobic methane oxidation by archaea in euxinic waters of the Black Sea. Organic Geochemistry 32, 1277-1281.
Seeberg-Elverfeldt, J., Schlüter, M., Feseker, T., Kölling, M., 2005. Rhizon sampling of pore waters near the sediment/water interface of aquatic systems. Limnology and oceanography: Methods 3, 361-371.
Soulet, G., Delaygue, G., Vallet-Coulomb, C., Bottcher, M.E., Sonzogni, C., Lericolais, G., Bard, E., 2010. Glacial hydrologic conditions in the Black Sea reconstructed using geochemical pore water profiles. Earth and Planetary Science Letters 296, 57-66.
Soulet, G., Menot, G., Bayon, G., Rostek, F., Ponzevera, E., Toucanne, S., Lericolais, G., Bard, E., 2013. Abrupt drainage cycles of the Fennoscandian Ice Sheet. Proc. Natl. Acad. Sci. U. S. A. 110, 6682-6687.
Soulet, G., Menot, G., Garreta, V., Rostek, F., Zaragosi, S., Lericolais, G., Bard, E., 2011a. Black Sea "Lake" reservoir age evolution since the Last Glacial - Hydrologic and climatic implications. Earth and Planetary Science Letters 308, 245-258.
Soulet, G., Menot, G., Lericolais, G., Bard, E., 2011b. A revised calendar age for the last reconnection of the Black Sea to the global ocean. Quaternary Science Reviews 30, 1019-1026.
Spivack, A.J., Palmer, M.R., Edmond, J.M., 1987. The sedimentary cycle of the boron isotopes. Geochimica et Cosmochimica Acta 51, 1939-1949.
Stoffers, P., Muller, G., 1972. Clay mineralogy of Black Sea sediments. Sedimentology 18, 113-121.
Underwood, M.B., Pickering, K.T., 1996. Clay-mineral provenance, sediment dispersal patterns, and mudrock diagenesis in the Nankai accretionary prism, southwest Japan. Clays and Clay Minerals 44, 339-356.
van Bodegom, P.M., Scholten, J.C.M., Stams, A.J.M., 2004. Direct inhibition of methanogenesis by ferric iron. Fems Microbiology Ecology 49, 261-268.
Vigderovich, H., Liang, L., Herut, B., Wang, F., Wurgaft, E., Rubin-Blum, M., Sivan, O., 2019. Evidence for microbial iron reduction in the methanic sediments of the oligotrophic southeastern Mediterranean continental shelf. Biogeosciences 16, 3165-3181.
Vigier, N., Decarreau, A., Millot, R., Carignan, J., Petit, S., France-Lanord, C., 2008. Quantifying Li isotope fractionation during smectite formation and implications for the Li cycle. Geochimica Et Cosmochimica Acta 72, 780-792.
Vorhies, J.S., Gaines, R.R., 2009. Microbial dissolution of clay minerals as a source of iron and silica in marine sediments. Nature Geoscience 2, 221-225.
Wallmann, K., Drews, M., Aloisi, G., Bohrmann, G., 2006. Methane discharge into the Black Sea and the global ocean via fluid flow through submarine mud volcanoes. Earth and Planetary Science Letters 248, 545-560.
Wegwerth, A., Ganopolski, A., Menot, G., Kaiser, J., Dellwig, O., Bard, E., Lamy, F., Arz, H.W., 2015. Black Sea temperature response to glacial millennial-scale climate variability. Geophysical Research Letters 42, 8147-8154.
Wegwerth, A., Kaiser, J., Dellwig, O., Shumilovskikh, L.S., Nowaczyk, N.R., Arz, H.W., 2016. Northern hemisphere climate control on the environmental dynamics in the glacial Black Sea “Lake”. Quaternary Science Reviews 135, 41-53.

Wilke, M., Farges, F., Petit, P.-E., Brown Jr, G.E., Martin, F., 2001. Oxidation state and coordination of Fe in minerals: An Fe K-XANES spectroscopic study. American Mineralogist 86, 714-730.
Xu, C.L., Greinert, J., Haeckel, M., Bialas, J., Dimitrov, L., Zhao, G.T., 2018. The Character and Formation of Elongated Depressions on the Upper Bulgarian Slope. Journal of Ocean University of China 17, 555-562.
Zander, T., Haeckel, M., Berndt, C., Chi, W.C., Klaucke, I., Bialas, J., Klaeschen, D., Koch, S., Atgm, O., 2017. On the origin of multiple BSRs in the Danube deep-sea fan, Black Sea. Earth and Planetary Science Letters 462, 15-25.
Zander, T., Haeckel, M., Klaucke, I., Bialas, J., Klaeschen, D., Papenberg, C., Pape, T., Berndt, C., Bohrmann, G., 2020. New insights into geology and geochemistry of the Kerch seep area in the Black Sea. Marine and Petroleum Geology 113, 104162.
Zhang, J., Dong, H., Liu, D., Fischer, T.B., Wang, S., Huang, L., 2012. Microbial reduction of Fe (III) in illite–smectite minerals by methanogen Methanosarcina mazei. Chemical Geology 292, 35-44.